5-2018

Novel Methodology for Emboli Analog Production and In-Vitro Simulation of Acute Ischemic Stroke

Anne Preut
University of Arkansas, Fayetteville

Novel Methodology for Emboli Analog Production and In-Vitro Simulation of Acute Ischemic Stroke

A thesis submitted in partial fulfillment
of the requirements for the degree of
Master of Science in Biomedical Engineering

by

Anne Preut
Kansas State University
Bachelor of Science in Chemical Engineering, 2016

May 2018
University of Arkansas

This thesis is approved for recommendation to the Graduate Council.

_____	_____
Morten O. Jensen, Ph.D., Dr.Med.	Jamie Hestekin, Ph.D.
Thesis Director	Thesis Director
_____	_____
Hanna K. Jensen, MD, Ph.D.	Kartik Balachandran, Ph.D.
Committee Member	Committee Member

Abstract

Stroke is the leading cause of disability and a primary cause of mortality, resulting in an estimated $33 billion dollars spent on healthcare, rehabilitation and lost productivity in the United States each year. The most prevalent cause of stroke incidents are acute ischemic events, manifested as blood clots in the vasculature supplying the brain. Current gold standard treatments have improved since 2006 with the introduction of mechanical stent retrievers; however, several issues with the current treatments to acute ischemic stroke remain. Thrombolysis of the clot with a tissue plasminogen activator may lead to weakening the vessel wall and consequently, hemorrhaging. Mechanical thrombectomy may result in clot fragmentation causing embolization downstream in a subsequent vessel. The proposed methodologies for emboli analog (EA) formation and in-vitro model for AIS simulation offer platforms for continued development of retrieval mechanism prototypes. EAs were developed in static and dynamic environments to compare composition and mechanical properties with cerebral thromboemboli mechanical and physiological properties. EAs formed at 50 RPM with a vertical rotator were found to be most similar in material stiffness to thromboemboli extracted from carotid endarterectomy (CEA) procedures ($p=0.972$). These EAs were also fibrin-rich, which clinical studies have found that fibrin-rich thromboemboli are linked to lower recanalization rates. Although the static EAs were not significantly different in material stiffness from CEA thromboemboli, they are homogenously composed of RBCs. An in-vitro model was created to simulate AIS physiological parameters including flow rate, temperature and vessel dimensions for prototype testing as well. A model of the vasculature was created using additive manufacturing and silicone to mimic cerebral vasculature including the middle cerebral artery, internal carotid artery and basilar artery where the majority of strokes occur.

Acknowledgements

Thank you to Dr. Morten Jensen and Dr. Jamie Hestekin for providing me with this research opportunity as well as the encouragement and advice along the way. I appreciate their trust in me to make this research project my own.

I would also like to thank Dr. Hanna Jensen and Dr. Kartik Balachandran for their expertise and guidance with this research and for their service on my thesis committee.

I would like to thank Dr. Tammy Lutz-Rechtin for safety advice with experiments and Phil Matsler for histological services.

I would like to thank the graduate and undergraduate students that provided input, advice and helping hands to complete this research including Garrett Easson, Megan Laughlin, Prashanth Ravishankar, John Kim, Edidiong Udofia, John Moore, Paolo Garcia, Amelia Falcon, Aksel Terkelsen, Tobias Dons, Fabien Capo, Mugisha Nitunga and Bailey Stinnett.

I would like to thank my Dad for his wisdom as well as prompting me to pursue engineering. I am grateful to my Mom for always being my cheerleader and thankful for the support of my siblings Sophie, Peter and Abel.

I would like to especially thank my husband and fellow engineering nerd Daniel for being able to adventure through life together.

Finally, I would like to thank God for designing a world to be explored and questioned.

Table of Contents

1 Introduction

1.1 *Clinical Relevance*

Approximately 800,000 people experience a new or recurrent stroke annually translating to a stroke occurring every 40 seconds and a stroke-related death every 4 minutes (Mozaffarian et al., 2016). Acute ischemic stroke (AIS) accounts for nearly 90% of strokes (American Heart Association, 2016) and is typically caused by an embolus or thrombus occluding the middle cerebral artery (MCA), internal carotid artery (ICA) or the basilar artery (BA) (Schuhmann, Gunreben, Kleinschnitz, & Kraft, 2016). Arkansas, Mississippi, Louisiana, Tennessee as well as several other southeastern states lie in the "stroke belt" of the nation. Continuing and advancing stroke research and awareness is of particular importance in the "stroke belt," where the average stroke mortality is 20% higher than the rest of the United States (Mozaffarian et al., 2016). Current gold standard treatment of stroke include intravenous thrombolysis and mechanical thrombectomy (American Heart Association, 2015). While intravenous thrombolysis intends to dissolve the clot, mechanical devices aim to physically extract the entire clot. Each approach has provided significant improvements in stroke treatment, yet several issues remain.

Recombinant tissue plasminogen activator (tPA) is the only approved FDA approved drug to treat AIS (American Heart Association, 2015; Paramasivam, 2015). Blood thinners such as tPA may weaken the blood vessel wall, and consequently increase the risk of hemorrhage. The drug must be administered intravenously within 4.5 hours of the stroke onset (Paramasivam, 2015). Additionally, tPA is usually ineffective in completely dissolving a clot causing large vessel occlusion; therefore, mechanical thrombectomy must be employed to achieve recanalization (American Heart Association, 2015). Related to intravenous thrombolysis, sonothrombolysis is another method of recanalization in clinical trials. Issues with this method

include successful recanalization being achieved in less than half of patients treated, increased risk of hemorrhage, and resistance to lysis by platelet rich clots (Tomkins et al., 2015).

Mechanical devices used for endovascular thrombectomy in stroke patients have continued to improve since the introduction of the Merci® coil retrieval device (Stryker) was first approved in 2004 (Paramasivam, 2015). Other FDA approved devices include the TREVO® XP Provue retriever (Stryker), Penumbra© aspiration retrieval device (Penumbra Inc.) and Solitaire™ revascularization device (Covidien). The main issues with mechanical thrombectomy include clot fragmentation resulting in new emboli and lengthy procedures (Kurre et al., 2013). Clot fragmentation may cause a subsequent stroke further downstream, while longer surgical procedures relate directly to the increased risk of neurons dying from starvation of oxygen-rich blood. New emboli have been identified in 2-17% of procedures using thrombectomy or a combined approach of thrombectomy and tPA (Behme et al., 2014; Gascou et al., 2014; Kurre et al., 2013; Mokin, Setlur Nagesh, Ionita, Mocco, & Siddiqui, 2016). Emboli traveling to the anterior cerebral artery (ACA) were identified to impact motor or supplementary motor areas of approximately 3.8% of stroke patients (Kurre et al., 2013). Recent studies also found stent perforation (1%), stent dislocation (2%) and stent occlusion (5%) to be additional causes of concern related to mechanical thrombectomy (Behme et al., 2014; Mokin, Fargen, et al., 2016). The Cover accessory (Lazarus Effect) was designed to surround a stent retriever and prevent clot fragmentation as well as embolization, but failed to achieve recanalization in 9% of the trial cases (Mokin, Setlur Nagesh, et al., 2016).

The development of retrieval mechanisms must be engaged with appropriate emboli analogs (EAs) for prototype testing. Composition of thromboemboli is instrumental in understanding how a retrieval mechanism will respond while specifically focusing on red blood

cells (RBCs) and fibrin. RBC-rich thrombi, those having more than 64% erythrocytic material, are associated with successful reperfusion, while higher percentages of fibrin/platelet components are linked to unreperfused groups (Hashimoto et al., 2016). Similarly, Yuki et al. (2012) achieved recanalization for 100% of RBC-rich clots introduced into extracranial arteries in swine models versus 37.5% recanalization for fibrin-rich clots.

Clinical studies have reported a large variability of thromboemboli composition with ranges of 0-96% RBCs, 2-100% fibrin, 3-80%platelets, and 0-31% white blood cells (WBCs) (Boeckh-Behrens et al., 2016; Cline, Carpenter, & Rai, 2013; S. K. Kim et al., 2015; Liebeskind et al., 2011; Niesten et al., 2014). These findings confirm that a range of EA compositions must be tested to hone prototype designs of retrieval mechanisms for cerebral thromboemboli. Current EA models fail to include both composition analysis and mechanical testing to provide EAs with physiological and mechanical properties that mimic cerebral thromboemboli properties. Further examination of these models is located under the section 1.4 Current Emboli Analog Models.

Continued research on cerebral thromboemboli and EA material properties is also necessary to understand clot etiology. Blood flow is essential to fibrin network formation and therefore, thromboemboli composition and mechanical stability as well (O. V. Kim et al., 2014; Weisel & Litvinov, 2017). Once fragmentation of the thrombus occurs, an embolus may cause artery-artery embolism or cardioembolic stroke, which account for nearly 70% of strokes reported in literature (Chueh et al., 2011; Hashimoto et al., 2016; S. K. Kim et al., 2015; Marder et al., 2006; Niesten et al., 2014; Schuhmann et al., 2016; Sporns et al., 2017). Approximately 25% of the reported stroke cases were cryptogenic demonstrating a need to further explore clot etiology with emboli analogs.

Prototype testing also requires models that include realistic parameters from stroke patients such as volumetric blood flow rate, vessel diameter and length, tortuosity, and physiological temperature. Although animal models must be used prior to clinical trials, vessel dimensions and directions of blood flow in cerebral vasculature vary between animal models and humans. In-vitro simulation ensures that the prototype retrieval mechanism is tested with realistic human parameters. It also allows for flexibility of testing multiple vessel configurations as well as a high sample number prior to tests with animal models. An overview of published methodology to produce vessel phantoms is summarized in the subsequent section 1.3 Vasculature Models.

1.2 *Thrombus Formation*

Thrombus formation occurs when an atherosclerotic plaque ruptures and exposes the subendothelial matrix to initiate platelet recruitment to the injury site. The enzymatic reactions of the coagulation cascade results in thrombin activation of the platelets resulting in a platelet "plug" at the injury site as well as fibrinogen to become fibrin monomers (Fogelson & Neeves, 2015). As the enzymatic reactions continue on the activated platelets, fibrinogen binds to the activated platelets (Weisel & Litvinov, 2017). Activated factor XIII causes fibrin monomers to become fibrin polymers, which form the thrombus structure and trap RBCs and WBCs.

Fibrin formation, and therefore thrombus composition, is dependent on the volumetric blood flow rate. Under increasing wall shear rate, fibrin fibers will begin to align parallel to the flow direction (Onasoga-Jarvis et al., 2014). The authors also discovered that fibrin fiber diameter decrease with increasing wall shear rate (Onasoga-Jarvis et al., 2014). In Figure 1, images of fibrin fiber alignment and diameter impacted by a range of wall shear rates may be seen. Previous research noted by Weisel & Litvinov (2017) found that fibrin fiber orientation

affects mechanical properties of the clot. Furthermore, the shear force applied by the blood flow may impact the probability of clot fragmentation and cause an embolus to travel downstream, thus risking embolization (Weisel & Litvinov, 2017). These findings provide support for EAs to be formed under dynamic environments rather than initiating coagulation in a test tube or other static environment. Composition, namely fibrin formation and orientation, is dependent on flow conditions and therefore, will determine the material stiffness of the embolus.

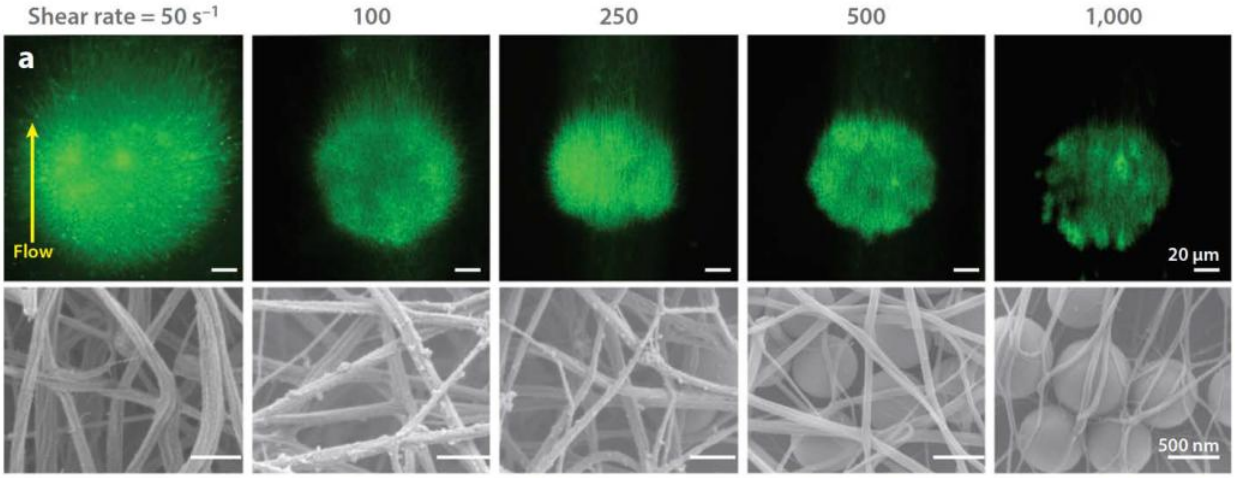

Figure 1. Fibrin fiber alignment and fiber diameter influenced by increasing wall shear rate (Onasoga-Jarvis et al., 2014)

1.3 *Vasculature Models*

Initially, an intracranial stroke model (Model #010S) was purchased through Vascular Simulations (Stony Brook, NY) for prototype testing of a retrieval mechanism. The vascular model is shown in Figure 2. For this model, the silicone vasculature is at most several millimeters in thickness. Additionally, it must be suspended in air to connect with a flow loop. The complexity and construction of the model discouraged use for preliminary prototype tests of a retrieval mechanism. Although this model realistically replicated the cerebral vasculature,

concern of puncturing the thin silicone vessels during prototype testing led to investigating simplified, alternative models.

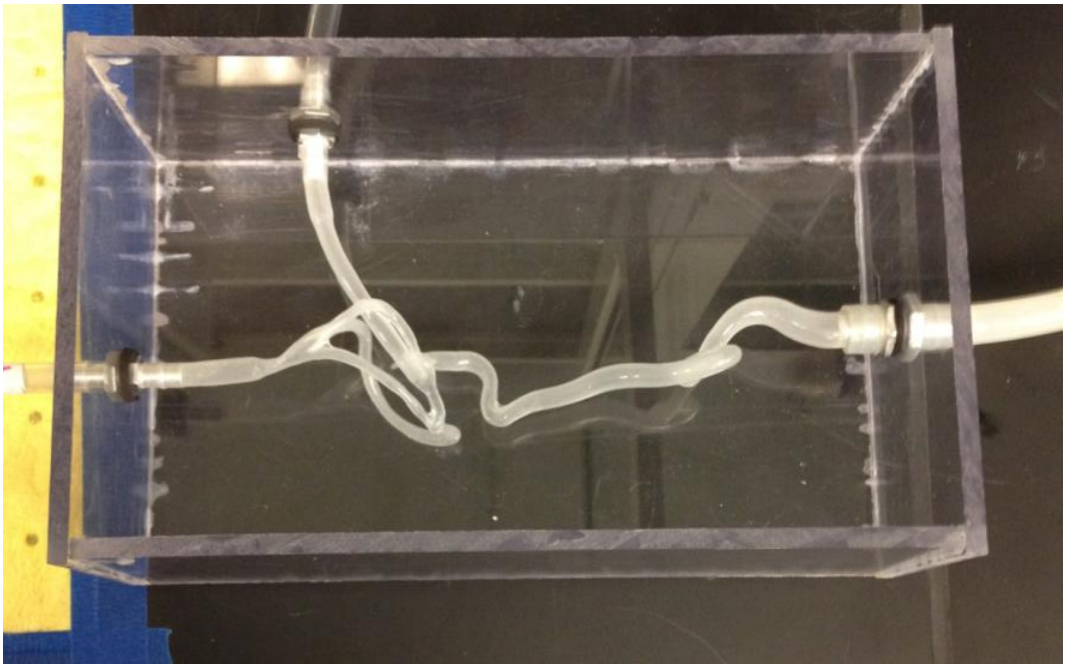

Figure 2. Intracranial stroke model purchased from Vascular Simulations (Stony Brook, NY)

In addition to Vascular Simulations, Shelley Medical Imaging Technologies (London, Ontario, Canada), Metal Professionals (South Range, WI), United Biologics (Tustin, CA), CIRS (Norfolk, VA) and Blue Phantom (Sarasota, FL) are companies that also fabricate similar vascular models used primarily for medical training. Purchasing vascular models from a company was avoided as they did not offer simplified vasculature and could not be easily replicated. Published methods on producing vascular models also offered several alternatives for fabricating a vascular phantom model in the laboratory. This provided the opportunity to replicate the phantom model and create a range of vessel geometries for prototype testing of a retrieval mechanism.

The published methods were, however, difficult to replicate as several required specific additive manufacturing equipment. For example, Ionita et al. (2014) used the Objet Eden 260V (Stratasys, Eden Prairie, MN) that can print in multiple materials including VeroClear, TangoPlus and SUP705, which were used to construct the phantom model. Although the authors have demonstrated an exceptionally accurate method to replicate patient vasculature, the use of specialized equipment limits the ability to replicate this specific method. Another published method required a multi-step process including an acrylonitrile butadiene styrene (ABS) core and shell mold, which was placed in a sodium hydroxide bath to remove support material and smoothed with xylene and 2-propanol (Chueh, Wakhloo, & Gounis, 2009). The authors then describe filling the void between the core and shell with silicone, allowing the silicone mold to cure and removing the ABS in a xylene bath. Others have used wax lumens covered by silicone and explored silicone coating methods such as a dip-spin procedure or painting layers on the wax lumen (Knox, Kerber, Singel, Bailey, & Imbesi, 2005; Seong et al., 2005; Sugiu et al., 2003; Wetzel et al., 2005). In this study, a new approach was undertaken to form a simple, reproducible cerebral vasculature model for prototype testing of a retrieval mechanism with EAs.

1.4 *Current Emboli Analog Models*

The primary aim of this work is to replicate cerebral emboli due to embolic strokes identified as the predominant etiology of AIS. Therefore, in-situ formation of clot analogs was not investigated with vascular models. Several in-vitro methods to form EAs have been published, but lack a complete picture including the mechanical properties and composition of each EA in comparison to cerebral thromboemboli. A recent method published by Kan et al.

(2010) resects a portion of a statically formed clot for emboli injection in swine models. Through manual elongation, the EAs stretched three times their original length, which demonstrated the elasticity and mechanical stability of the experimental thrombi (Kan et al., 2010). Metrics for composition analysis were qualitative – fibrin and RBCs layers in thrombi versus specific quantities of fibrin, RBCs and other components. Although Kan et al. (2010) demonstrated a new method to prepare EAs, the lack of quantitative analysis limits comparison with thromboemboli retrieved from human stroke patients.

Duffy et al. (2016) provides a method for EAs with calculated ranges of fibrin, WBCs and RBCs, but lacks information on the material stiffness of each EA. Interestingly, Duffy et al. (2016) found that implementing dynamic conditions with a modified Chandler loop produced a higher fibrin content of 80% in whole blood clots versus 10% fibrin content in clots made in static conditions. Based on human, porcine and bovine blood, Chueh et al. (2011) offer EAs similar in material stiffness to the thromboemboli extracted from carotid endarterectomy (CEA) and AIS patients, but found their EAs were homogeneously composed of RBCs. A reproducible method for creating EAs is necessary for prototype testing of stroke retrieval devices, and requires that the results consistently mimic the desired material stiffness and composition of cerebral thromboemboli.

1.5 *Specific Aims and Hypotheses*

(1): **Develop emboli analogs that mimic material stiffness of stroke thromboemboli.** It is hypothesized that a dynamic system will effectively mimic the in-vivo environment appropriate for EA formation and offer an EA with similar mechanical properties to stroke thromboemboli. Additionally, it is hypothesized that measuring and combining specific

quantities of plasma, RBCs, platelets and thrombin is unnecessary to mimic mechanical properties and that whole blood may be used to induce clot formation. First, mechanical differences between EAs formed in static and dynamic environments must be understood. Second, the relationship between the material stiffness and the speed of the vertical rotator, and therefore, the shear stress applied to the clot must be examined as well. Results are compared to published data on the mechanical properties of human cerebral thromboemboli.

(2): **Alter emboli analog physiological properties to be fibrin-rich**. It is hypothesized that a dynamic environment induces fibrin-rich EAs and may be adjusted to produce a range of EA compositions for prototype testing. Histology of tissue samples for static and dynamic environments is analyzed for percent composition of fibrin and RBCs as they are the main components in thromboemboli. Composition analysis for EAs formed in a range of dynamic environments provides a deeper understanding of the differences in their mechanical properties.

(3): **Establish in-vitro model to simulate AIS**. The key parameters to establish for this model include physiological temperature, volumetric flow rates and vessel dimensions. The proposed method offers a platform to replicate cerebral vasculature tortuosity and inner diameters of the arteries.

2 Methodology

2.1 *Formation of Emboli Analogs*

To create EAs, porcine blood was exclusively used, as it is an excellent candidate due to its similarities to human blood. Specifically, Chueh et al. (2011) found porcine clots resemble the mechanical stiffness of human stroke clots. Porcine blood anticoagulated with sodium citrate was obtained from Lampire Biological Laboratories (Pipersville, PA). Totaling a volume of 3 mL, a 9:1 ratio of whole blood and 2.45% (w/v) calcium chloride was pipetted into polyvinyl tubing, which was closed with a short silicone piece fitted over the polyvinyl tubing. Polyvinyl tubing inner diameter and length were 6.35 mm and 22 cm, respectively.

Either dynamic or static environments initiated coagulation. A dynamic environment was created through a modified Chandler loop technique, which mimics the dynamics of blood flow. As seen in Figure 3, a custom tubing holder was fabricated to attach to a digital Cole-Parmer MasterFlex® peristaltic pump (Model 7523-50, Vernon Hills, IL). The tubing was placed equidistance from the central point of rotation. In the dynamic environment, coagulation also occurred for one hour, while the RPM of the vertical rotator was adjusted to the following values: 34 RPM, 50 RPM and 80 RPM. As the blood volume was 3 mL, an estimate of the volumetric blood flow rate may be calculated for each RPM as follows: 102 mL/min (34 RPM), 150 mL/min (50 RPM) or 240 mL/min (80 RPM). These values were chosen based on flow rates experienced in the ICA (240mL/min), MCA (121 ± 28 mL/min) and BA (100-200 mL/min) (Kandel, Schwartz, & Jessell, 2000; Oktar et al., 2006; Stock, Wetzel, Lyrer, & Radü, 2000). Regarding static conditions, contents of the tubing were briefly mixed and left stationary for one hour on a rod extended from a support stand to ensure emboli analogs formed parallel to the

ground. An example of the static environment setup is shown in Figure 4 where five static EAs were formed simultaneously.

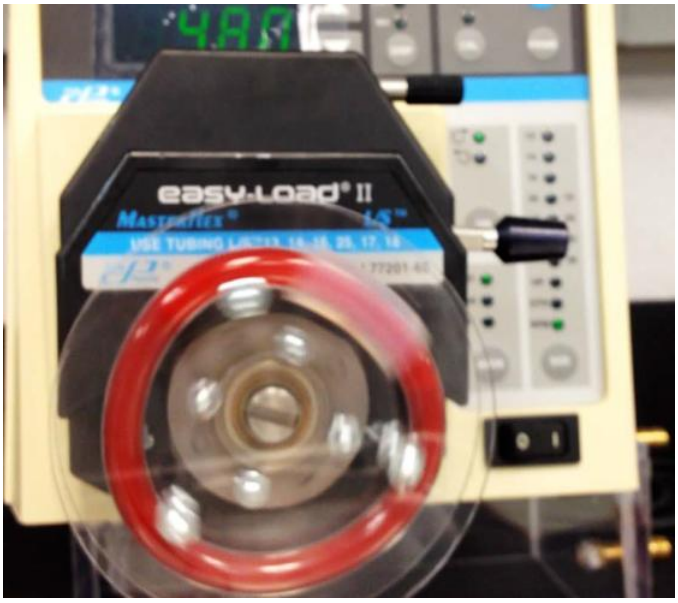

Figure 3. Vertical rotator used for inducing dynamic environment for emboli analog production.

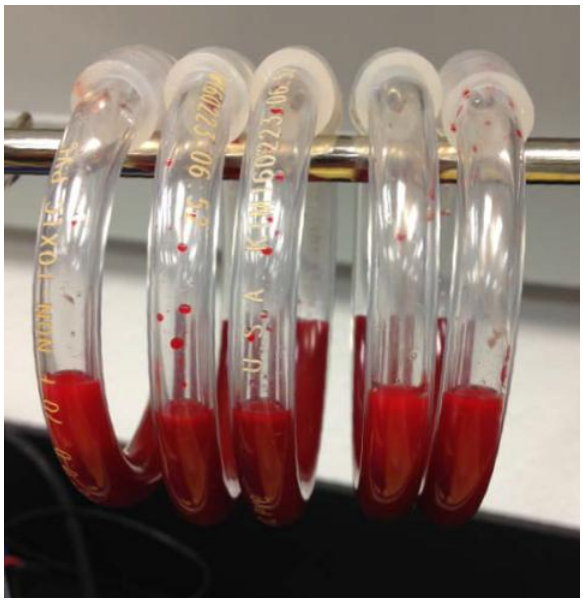

Figure 4. Five replicates of emboli analogs formed in static environment.

Once EA formation was complete, each EA was removed from the tubing and rinsed with phosphate-buffered saline (PBS) solution prior to obtaining weight and dimension measurements. Static EAs were especially difficult to remove and remained attached to the tubing wall. This required the EAs to be flushed from the tubing with PBS. In certain cases, the static EA remained on the tubing wall and required the tubing wall to be cut with a utility knife. Once the tubing was opened, the EA was extracted with tweezers. All clots were aged in PBS for approximately 24 hours following methods previously established for mechanical testing of EAs (Chueh et al., 2011). One study used EAs for up to 3 weeks for composition analysis (Duffy et al., 2016); therefore, material stiffness of emboli analogs was compared for two storage

conditions. Ten EAs formed sequentially at 150 mL/min were used to compare material stiffness after 24 hours (n=5) in PBS at room temperature and 1 week (n=5) in PBS at 4 °C.

2.2 *Emboli Analog Measurements*

EAs were measured before and after storage in PBS. Final measurements reported are from the length and width of stored EAs. Once the EAs had been stored for approximately 24 hours, the EA was removed from the storage container and blotted with a Kimwipe tissue to remove excess liquid. The mass of each EA was recorded with a digital scale while the length and width of the EA was recorded with a standard ruler.

2.3 *Emboli Analog Dissection*

Following EA measurements, dissection of EAs for compression testing was performed using a dissection microscope and ruler. EAs dissected transversely resulted in small cylindrically shaped tissue segments with an approximate height of 2 mm. Due to the heterogeneity of the EAs, at least two sections provided an average material stiffness for each EA. Prior to compression testing, a caliper was used to measure the diameter and height of each tissue section.

2.4 *Biomechanical Compression Testing of Emboli Analogs*

For direct comparison with published biomechanical testing results on the material stiffness of human thromboemboli and previous methods for emboli analog formation, the compression testing method of Chueh et al. (2011) was closely followed using an Instron 3300 (Instron, Norwood, MA) and load cell of 2 kN. Tissue samples were subjected to a force ramp

rate of 0.5 N/min. It is to be noted that a submersion compression clamp was not available for use and compression tests were performed at room temperature. Tissue samples were centrally placed on the compression disk. Two examples of the tissue segments from static and dynamic EAs are shown in Figure 5. Bluehill® Universal Software (Instron, Norwood, MA) collected compression testing data at a sampling rate of 10 Hz.

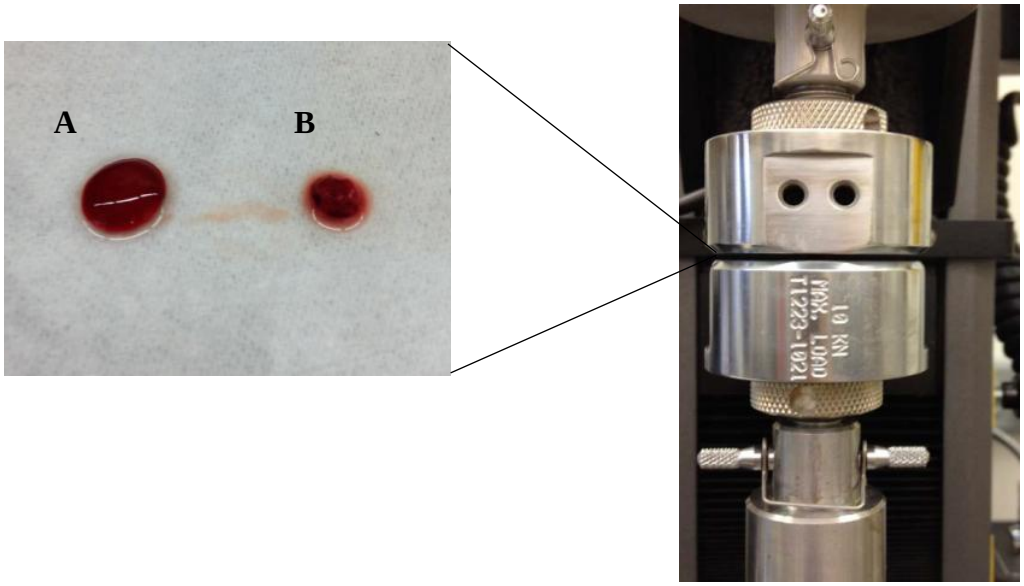

Figure 5. Tissue sections from static (left A) and dynamic (left B) environments were individually placed between Instron grips (right) for compression testing.

Young's modulus was calculated for 75-95% strain, ε, with the key assumption that the stress-strain relationship is linear and therefore, the EAs are acting as a purely elastic material for $0.75 < \varepsilon < 0.95$. The following equation was used to calculate Young's Modulus, $E_{75\text{-}95\%}$:

$$\sigma = E_{75-95\%} * \varepsilon \qquad \text{Equation 1}$$

2.5 *Histology*

Aged EAs were placed in 10% formalin for 48 hours, dehydrated and sectioned for hematoxylin and eosin (H&E) staining. All histology samples were processed by a trained histologist in the Department of Poultry Science at the University of Arkansas. As composition of static EAs has been reported, these values were compared to results from EAs formed in the three aforementioned dynamic environments. Stained tissue sections were imaged with a Nikon Eclipse Ci-L/S Microscope (Japan) and analyzed for fibrin/platelet to red blood cell ratios with a custom MATLAB code, which will be discussed in the section 2.5.1 Composition Analysis. At least three EAs of each dynamic environment were formed and processed to obtain a minimum of three sections per clot. Three EAs were formed at 34 RPM, five at 50 RPM and four at 80 RPM. Tissue sections were imaged and analyzed to provide an overall composition percentage of fibrin/platelets and RBCs for EAs formed at 34 RPM (n=14), 50 RPM (n=23) and 80 RPM (n=12).

Static EA tissue sections were difficult to obtain completely intact as the center of the section was frequently washed out. This pointed towards the tissue remaining unfixed in the center. Therefore, static EAs were quartered for the fixation process and then brought to histology, but exhibited similar issues. Thicker sections were cut; however, the tissue appeared cracked and composition analysis could not be formed. Due to similarity in static EA formation with the procedure established by Duffy et al. (2016), composition analysis of their static EAs were used for comparison with histology results from the dynamic EAs discussed.

2.5.1 *Composition Analysis*

From images of H&E stained tissue sections, normalization and color deconvolution produced images specific to hematoxylin and eosin stained components. To minimize bias from staining and imaging differences, a reference matrix provided stain vectors to normalize the images for direct comparison (Veta, 2015). The method of image normalization is based on the algorithm from Macenko et al. (2009) and code describing Macenko's algorithm (Khan, 2015; Veta, 2015). Normalization of the image begins with converting the original image (Figure 6) into its optical density (OD) image (Figure 7) as follows:

$$OD = -\log\left(I/I_0\right) \qquad \text{Equation 2}$$

where the image intensity (I) is divided by the light intensity entering the slide (I_0), which is 255.

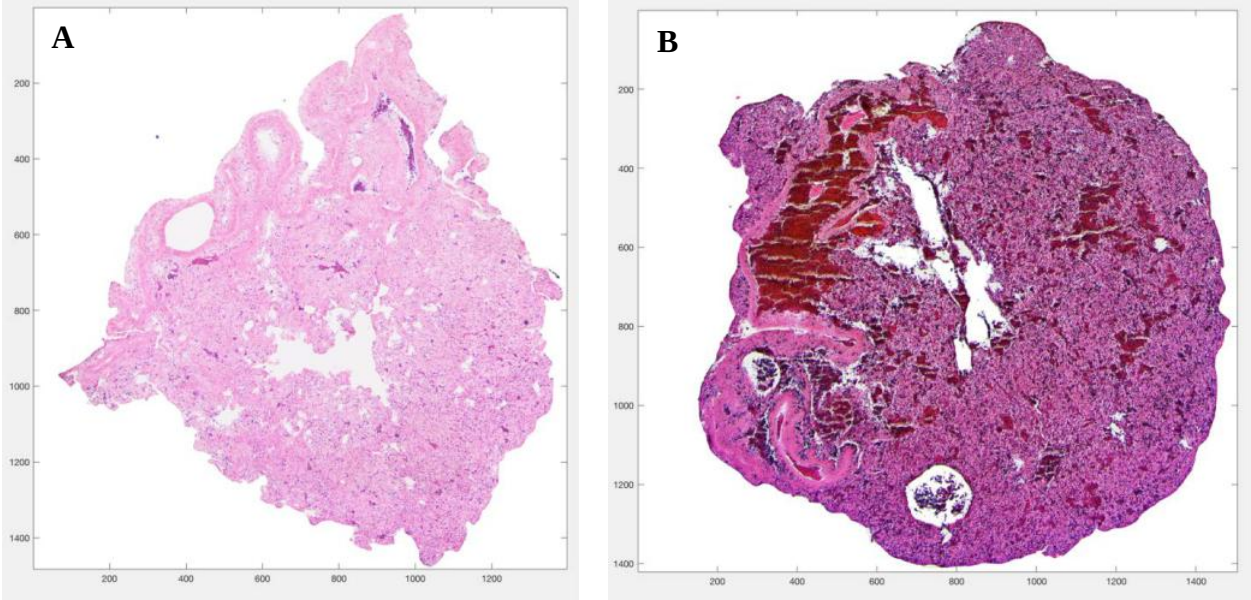

Figure 6. H&E stained sections of dynamic EAs. (A) EA formed at 80 RPM demonstrates a lightly stained tissue as well as a fibrin-rich section and (B) EA formed at 34 RPM that represents overstained tissue and mixed composition of fibrin and RBCs. Vertical and horizontal axes indicate image dimensions in pixels.

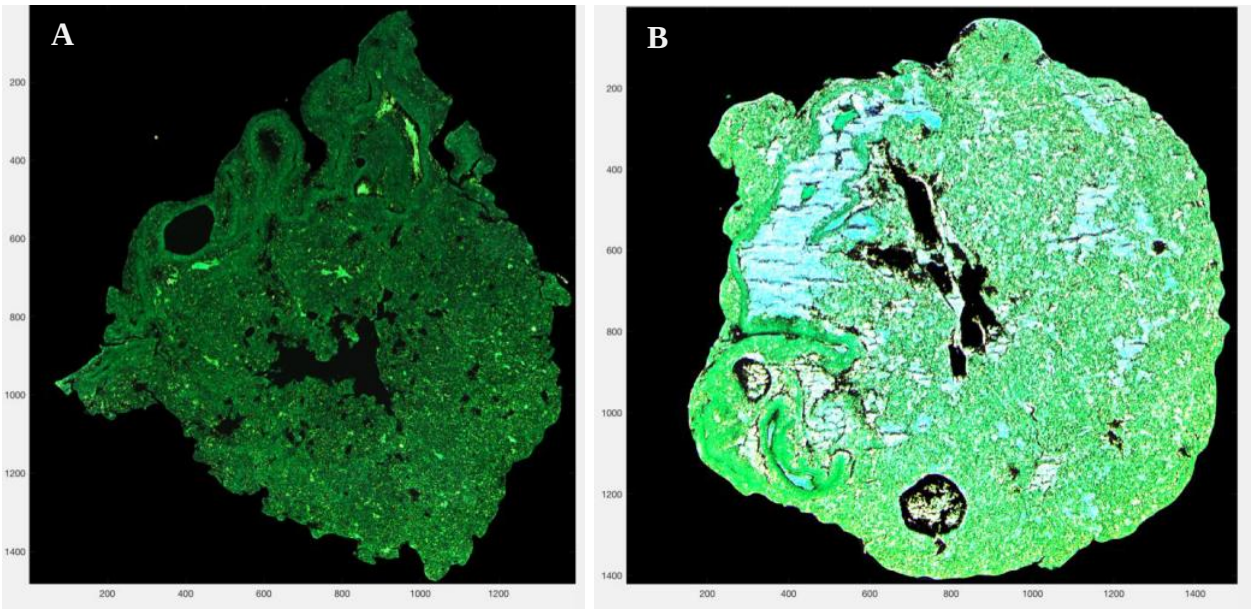

Figure 7. Optical density (OD) images of tissue sections from (A) EA formed at 80 RPM and (B) EA formed at 34 RPM. Axes indicate image dimensions in pixels.

The OD matrix must be reshaped to have three columns that correspond to values in the red, green and blue channels. The low OD values with a threshold of 0.15 are removed from the matrix (Macenko et al., 2009). The right eigenvectors calculated from the OD matrix create a plane based on the two largest eigenvalues where the OD pixels are then projected onto that plane. The angle between each pixel and the first eigenvector are calculated to create scalar values at each point. The 1st and 99th percentile of the angles provide the angle extremes which can be converted back to OD space and provide stain vectors corresponding to hematoxylin and eosin. These are the stain vectors that can replace the original reference matrix if a specific reference image is desired.

Color deconvolution is based on a previously established method and additional work describing this method (Ruifrok & Johnston, 2001; Veta, 2015). Once the stain vectors are calculated, the OD matrix (M) is formed first with the largest stain vector, which corresponds to hematoxylin, and second with the smaller stain vector, which corresponds to eosin. The two stain concentrations (C) are calculated based on the following equation:

$$C = M^{-1}[y] \qquad \text{Equation 3}$$

where y corresponds to the OD image after reshaping, but prior to thresholding. The concentrations may then be multiplied by the reference matrix and its exponential produces images of the hematoxylin-stained components and the eosin-stained components (Figure 8).

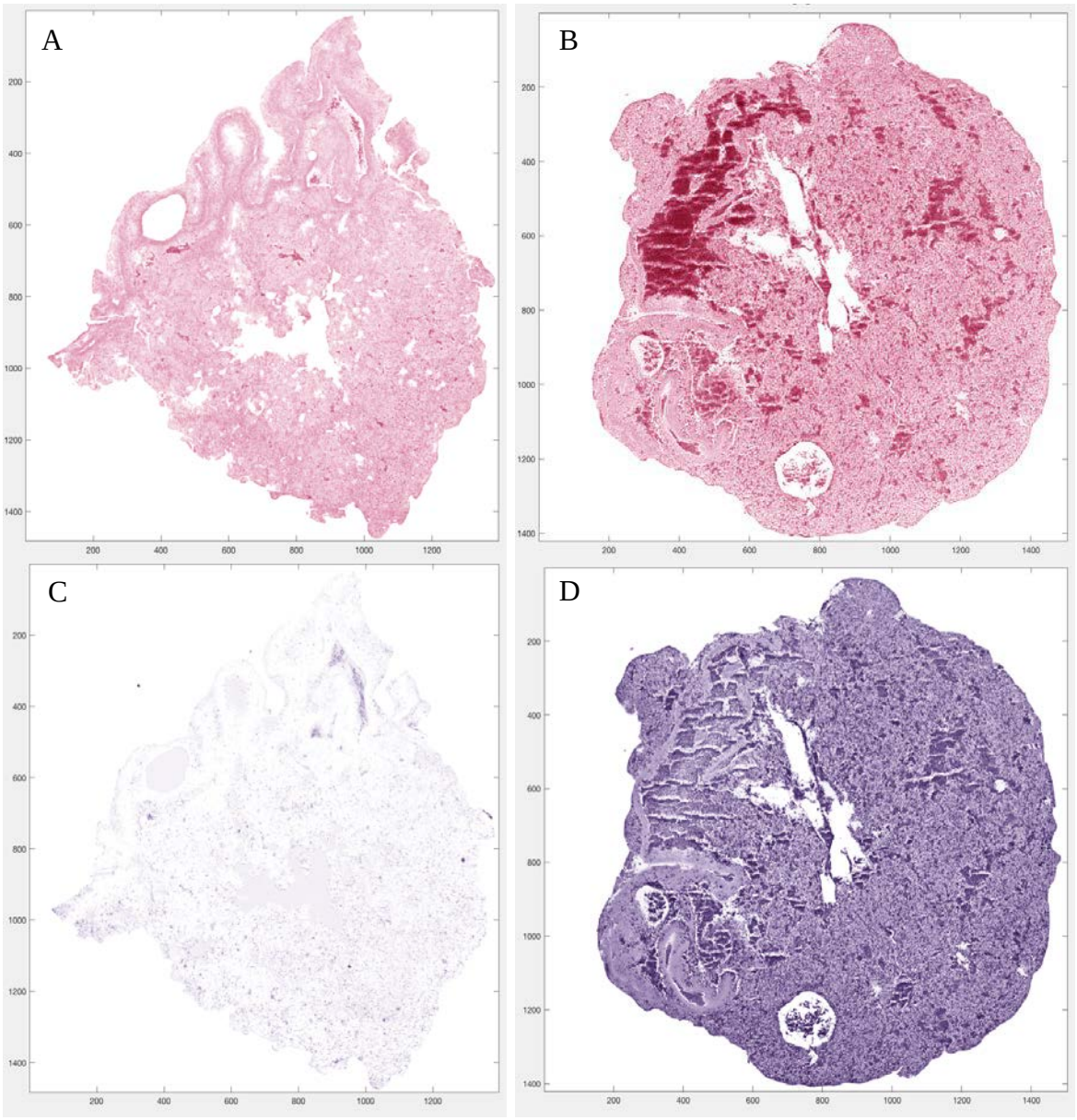

Figure 8. Color deconvolution results in (A) eosin stained image of EA formed at 80 RPM, (B) eosin stained image of EA formed at 34 RPM, (C) hematoxylin stained image of EA formed at 80 RPM and (D) hematoxylin stained image of EA formed at 34 RPM.

Fibrin and RBCs are the main components of thrombi but are both stained pink-red with eosin. The eosin-stained image provides a platform to extract the composition data based on fibrin and RBCs. A threshold of 0.97 for the red channel of the eosin-stained image removes a

majority of white space in the image and results in background masks as seen in Figure 9. This ensures that the composition analysis is performed only on pixels represented by tissue that absorbed eosin. The threshold was manually adjusted and qualitatively analyzed for the optimal threshold that removes a majority of white space without removing the lightly-stained fibrin.

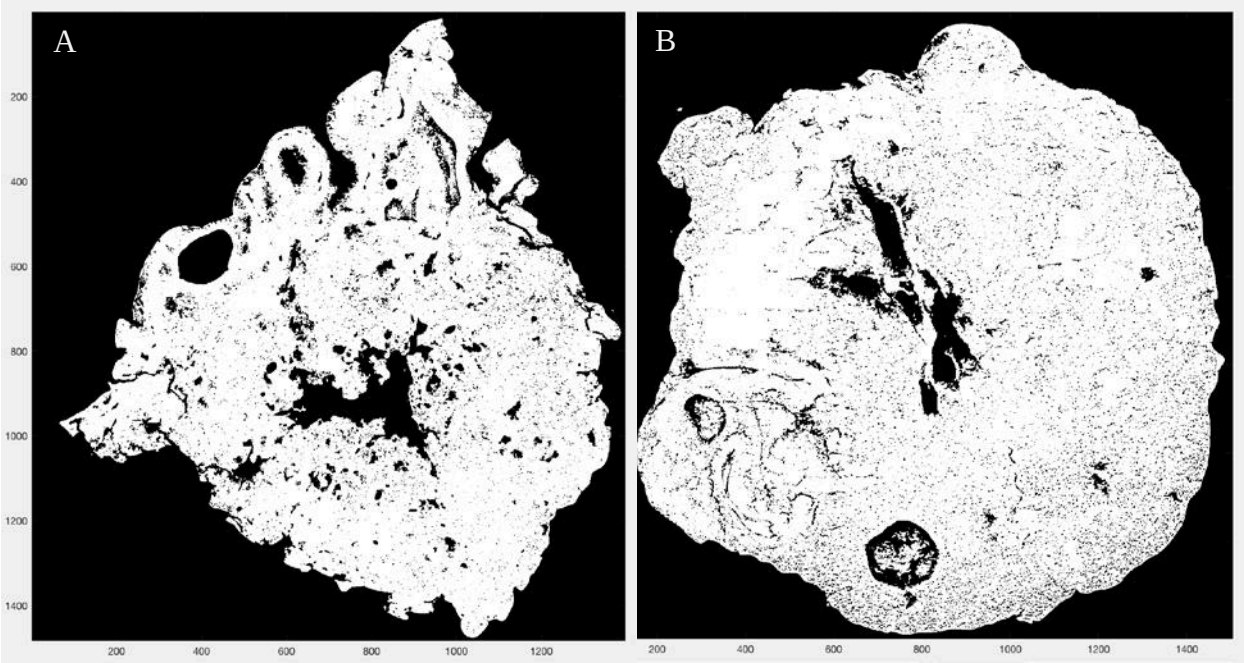

Figure 9. Background masks of EAs formed at (A) 80 RPM and (B) 34 RPM completely remove pixels representing white or lightly colored background to ensure background pixels are not included in the individual summations of fibrin and RBC pixels.

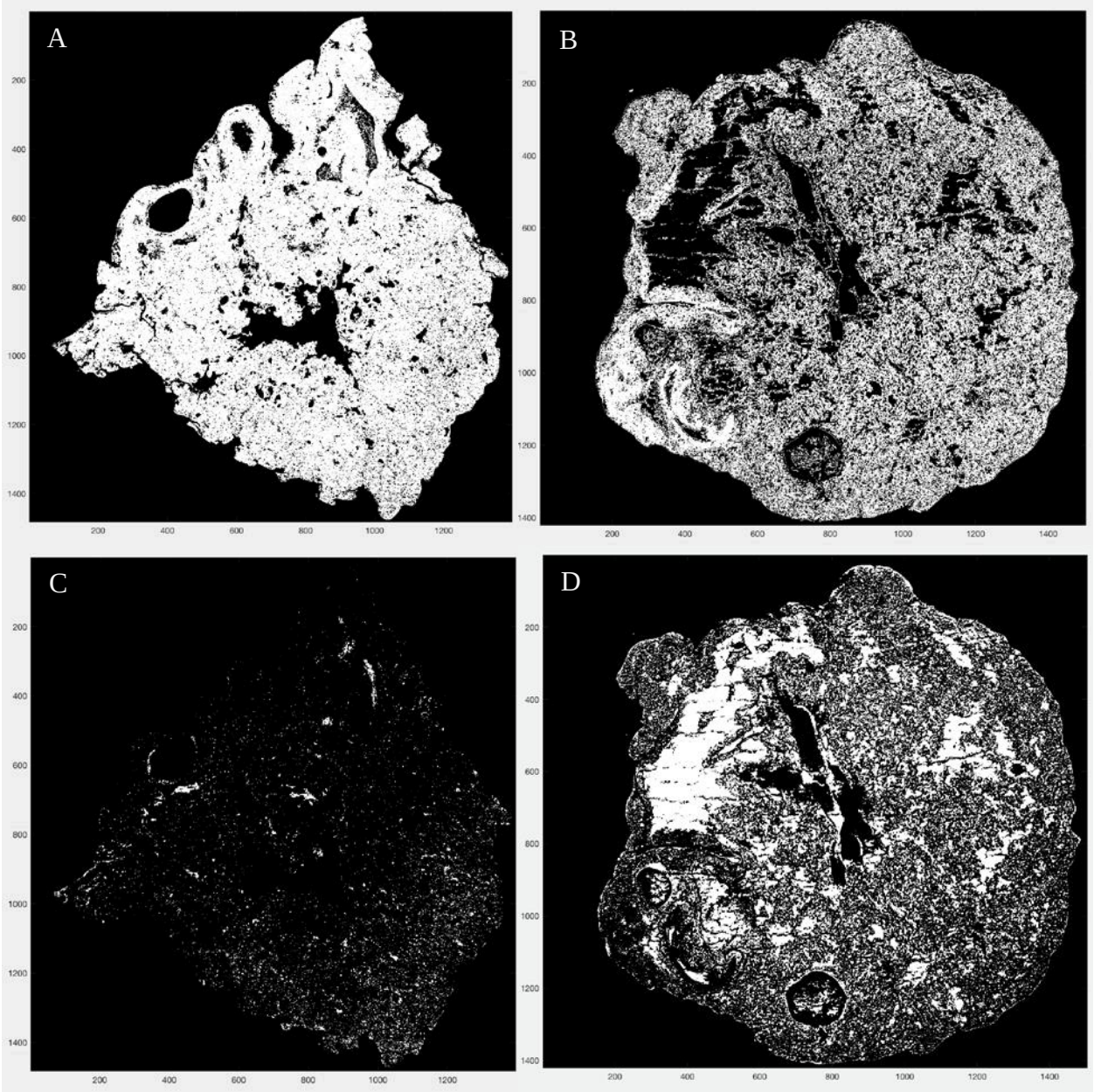

Figure 10. Masks represented by white space or 1's in the matrix are equivalent to (A) fibrin in EA formed at 80 RPM, (B) fibrin in EA formed at 34 RPM, (C) RBCs in EA formed at 80 RPM and (D) RBCs in EA formed at 34 RPM.

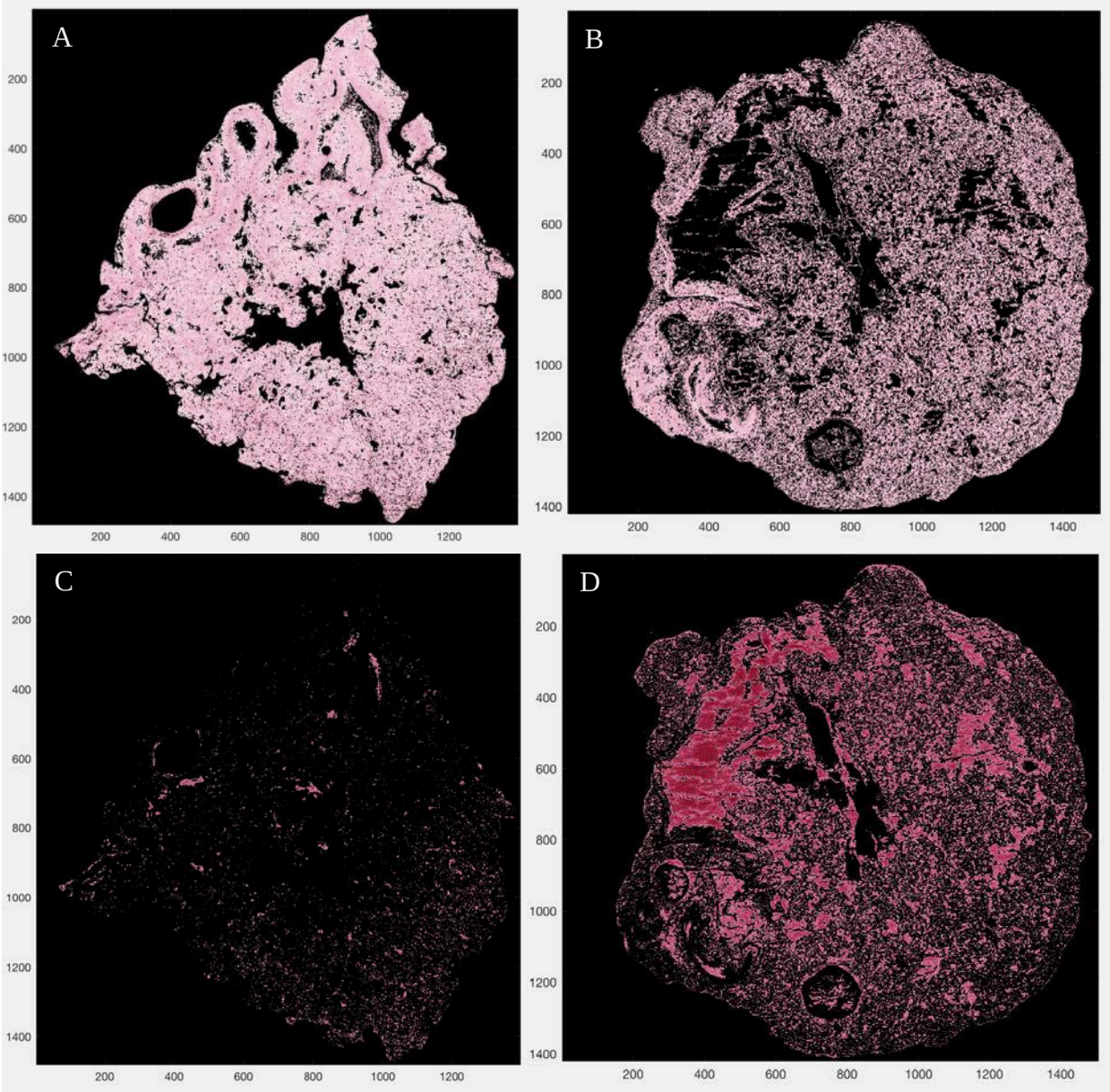

Figure 11. Masks overlaid on eosin stained images represent (A) fibrin in EA formed at 80 RPM (B) fibrin in EA formed at 34 RPM, (C) RBCs in EA formed at 80 RPM and (D) RBCs in EA formed at 34 RPM.

Then, a threshold separating the two average intensity values produces two masks to correspond with either fibrin/platelets or RBCs. Given the masks are matrices of zeros and ones, the ones may be summed together to compute the number of pixels that correspond respectively to fibrin/platelets and RBCs. These masks may be seen in Figure 10. Dividing these by the total number of pixels relative to the tissue in the image, a composition percentage for RBCs as well as fibrin/platelets may be calculated. Through comparison of resulting mask images over the eosin-stained tissue, a common threshold of 0.87 was identified in the red channel of the images to separate out the fibrin/platelet pixels from the RBC pixels. Masks overlaid on the eosin-stained images are shown in Figure 11.

This method was unable to properly calculate composition percentages for seven tissue sections for unknown reasons. Five of the seven sections were clearly fibrin-rich tissue sections, yet the method identified over 50% of the tissue section as RBCs. Therefore, calculations from these tissue sections were discarded. After these were discarded, each EA still had at least three tissue sections for comparison, which allowed for composition analysis for 87% of the H&E stained tissue slides. The MATLAB code written for the composition analysis is documented in Appendix A.

2.6 ***Flow System***

2.6.1 *Design Criteria*

The key parameters to establish for this model include temperature and volumetric flow rates. The temperature of the system must correspond to the body's natural temperature of 37˚C (98.6 ˚F). As previously mentioned, the MCA mean flow rate is 121 ± 28 ml/min and the ICA mean flow rate is 240 ml/min, while the BA mean flow rate lies between 100-200 ml/min

(Kandel et al., 2000; Oktar et al., 2006; Stock et al., 2000). Pressures and flow rates experienced during a stroke will occur once an embolus is introduced into the in-vitro stroke model. This system must incorporate the vessel model to allow for embolization with EAs and prototype testing for stroke research.

2.6.2 *Implementation*

Instrumentation used to simulate, control and monitor the AIS parameters of the completed system is shown in Figure 12. The temperature of the water bath was adjusted to correspond to physiological temperature within the flow loop. Styrofoam peanuts were layered on the water within the water bath to provide additional insulation and prevent heat loss. A high accuracy J/K dual input thermocouple thermometer HH802U (Omega, Norwalk, CT) measured the temperature of the water bath and inlet temperature of the vessel model. Masterflex® C-flex Ultra L/S 17 Tubing (Cole-Parmer, Vernon Hills, IL) was used with a digital peristaltic pump (Model 7523-50, Cole-Parmer, Vernon Hills, IL) to pump distilled water from a glass container placed within the water bath to the flow loop system. Due to the pulsatile flow, a pulse dampener (Cole-Parmer, Vernon Hills, IL) was necessary to ensure accurate flow rate readings from a SRI-2 Indicator (Flow Technology Inc., Phoenix, AZ) connected to a turbine flow meter (FT0-3, Flow Technology Inc., Phoenix, AZ).

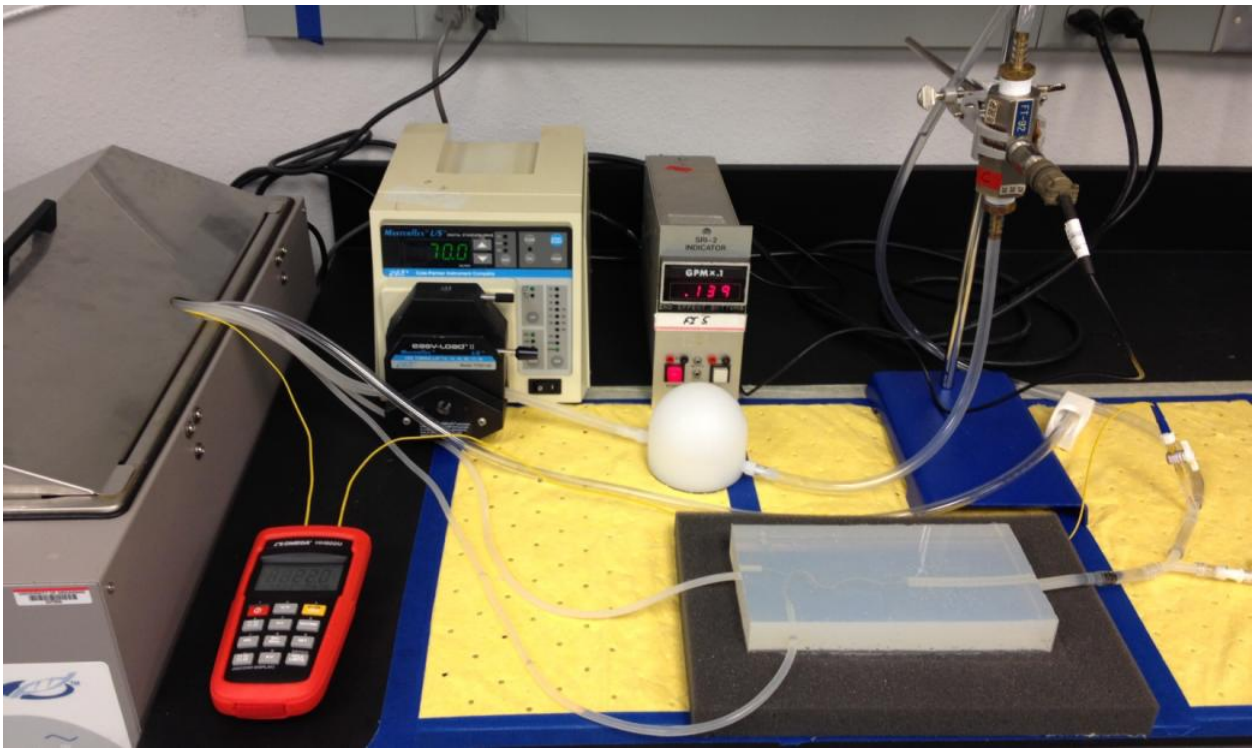

Figure 12. Instrumentation used to simulate, control and monitor the AIS parameters of the in-vitro system

After the pulse dampener, polyvinyl tubing was primarily used apart from silicone tubing immediately prior to and after the silicone model. A t-shaped connector after the flow meter linked additional tubing to form a bypass and eliminate pressure build-up once an EA would be introduced to the system and stop fluid flow for prototype testing. Another t-shaped connector provided a port for one of the thermocouples to measure inlet temperature of the silicone vascular model (Figure 13). This was immediately followed by a y-shaped connector that acted as point to introduce an EA as well as a retrieval mechanism to the model. Specifics of the silicone vascular model will be discussed in the subsequent section 2.7 Silicone Mold of Cerebral Arteries.

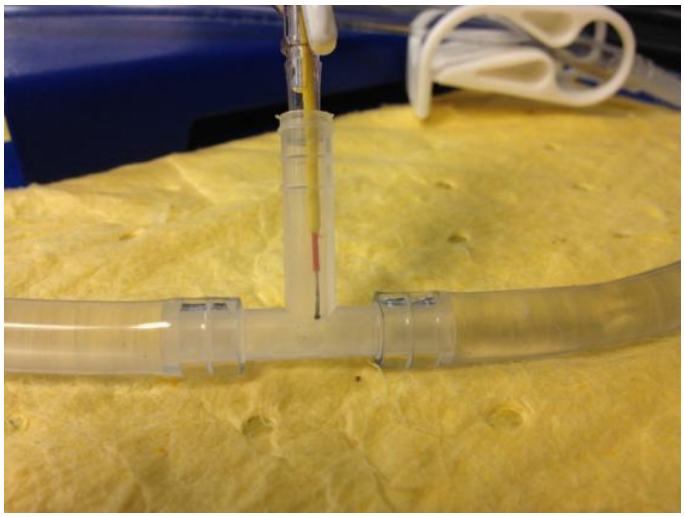

Figure 13. Thermocouple measures temperature at vascular model inlet within t-connector

2.7 *Silicone Model of Cerebral Arteries*

2.7.1 *Design Criteria*

Of 531 patients from 11 clinical studies, the location of occlusion occurred in the MCA most frequently at 56.7% followed by the ICA at 33.7%, BA at 7.2%, posterior cerebral artery (PCA) at 3.0% and anterior cerebral artery (ACA) at 0.4% (Boeckh-Behrens et al., 2016; Chueh et al., 2011; Cline et al., 2013; Hashimoto et al., 2016; S. K. Kim et al., 2015; Krajíčková et al., 2017; Liebeskind et al., 2011; Marder et al., 2006; Niesten et al., 2014; Schuhmann et al., 2016; Simons, Mitchell, Dowling, Gonzales, & Yan, 2015). As the PCA and ACA incur a small percentage of strokes, the MCA, ICA and BA were chosen to be replicated with a cerebral vasculature void in a silicone mold. The design criteria based on the MCA, ICA and BA included vessel diameter, length and tortuosity. The mean vessel diameter of the MCA is 2.8 mm (0.11 in), while the ICA mean diameter is 5.1 mm (0.20 in) and the BA mean diameter is 3.2 mm (0.12 in) (Oktar et al., 2006; Smoker, Price, Keyes, Corbett, & Gentry, 1986; Stock et al., 2000).

Another design criterion was to ensure that the vasculature model could be easily replicated as well as altered to produce alternative cerebral or cardiovascular models.

2.7.2 *Implementation*

Chemical and heat treatments are common to remove one material while leaving the desired material behind. Both were explored regarding ballistics gel, silicone and available materials for additive manufacturing such as ABS and polylactic acid (PLA). Ballistics gel was found to have too low of a melting temperature in comparison to PLA and ABS whereas the melting temperature difference between silicone, ABS and PLA offered a possibility of using a heat treatment. Investigating solubility properties of ABS and PLA with silicone offered a safe, simple alternative to a heat treatment.

Modeling of the desired vessels in SolidWorks resulted in a lumen 3D printed in ABS with an Ultimaker (Ultimaker B.V., Geldermalsen, Netherlands). The lumen print was suspended in a customized acrylic box and covered with platinum cure silicone (Raw Material Suppliers, San Marcos, CA). Silicone was allowed to cure overnight at room temperature and then chemically treated to remove the ABS lumen material. Due to proprietary information, the specifications of the chemical treatment are not discussed. Two iterations of a silicone mold were completed due to the first prototype incurring bubbles in the cured silicone hindering a clear view of the vessel and design changes to the tortuosity as well as the connection between the flow loop tubing and vessel model.

2.8 *Statistical Analysis*

Outliers from compression testing were removed with Grubbs' test in GraphPad QuickCalcs (San Diego, CA). Subsequently, statistical significance between groups was found with *t* test also in GraphPad QuickCalcs (San Diego, CA). Values are reported in terms of mean +/- standard deviation unless otherwise specified.

3 Results

3.1 *Emboli Analog Dimensions*

Length and width of EAs formed in each environment were averaged for comparison with human stroke thromboemboli retrieved in a clinical study by Marder et al. (2006). Dynamically formed EAs had a length of 15.1 +/- 9.4 mm and width of 3.1 +/- 0.6 mm, which most closely resembled stroke thromboemboli retrieved from the ICA with a length of 10.1 +/- 10.2 mm and width of 2.8 +/-1.2 mm (Marder et al., 2006). Those from the MCA had a length of 3.1 +/- 1.5 mm and width of 1.8 +/- 0.8 mm (Marder et al., 2006). Static EAs with a length of 65.7 +/- 2.9 mm were twice the maximum length of emboli retrieved by Marder et al. (2006) in their study of 25 patients. Average width of the static EAs was 4.7 +/- 0.6 mm. Figure 14 demonstrates the heterogeneity of the dynamic EAs versus the homogeneous static EAs. From the 1-3 mm mark of Figure 14A, compacted RBCs may be seen within the fibrous structure. While the dynamic EAs were flexible, they maintained their shape longitudinally and transversely. Once the static EAs were removed from the tubing, they flattened slightly into an oblong shape in the transverse direction.

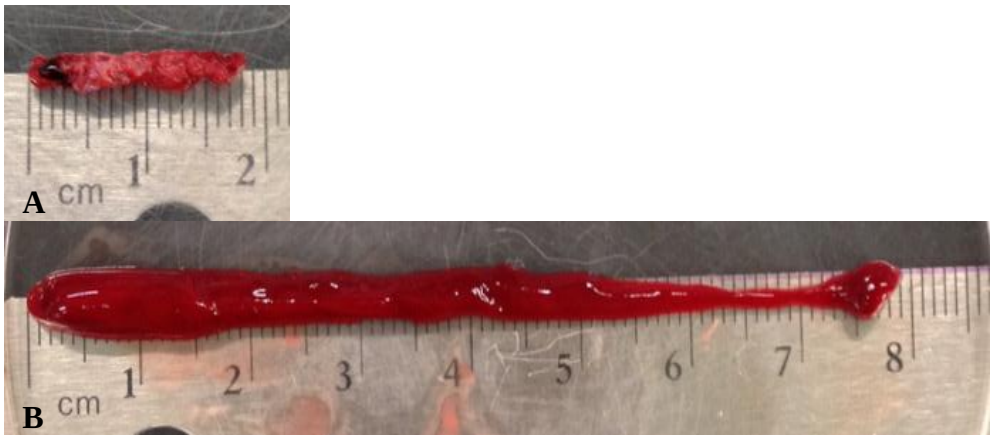

Figure 14. Images of (A) dynamically formed emboli analog and (B) static emboli analog.

3.2 *Emboli Analog Material Stiffness*

3.2.1 *Storage Conditions*

Material stiffness of emboli analogs stored for 24 hours and 1 week in saline determined the feasibility of storing clots long-term for continued use in prototype testing. Figure 15 demonstrates that a two-fold increase in material stiffness was found between EAs stored for 24 hours and 1 week. The average $E_{75-95\%}$ values for 24 hour and 1 week storage were 1.57 +/- 0.35 MPa and 3.30 +/- 1.84, respectively and did not show statistical significance (p=0.07).

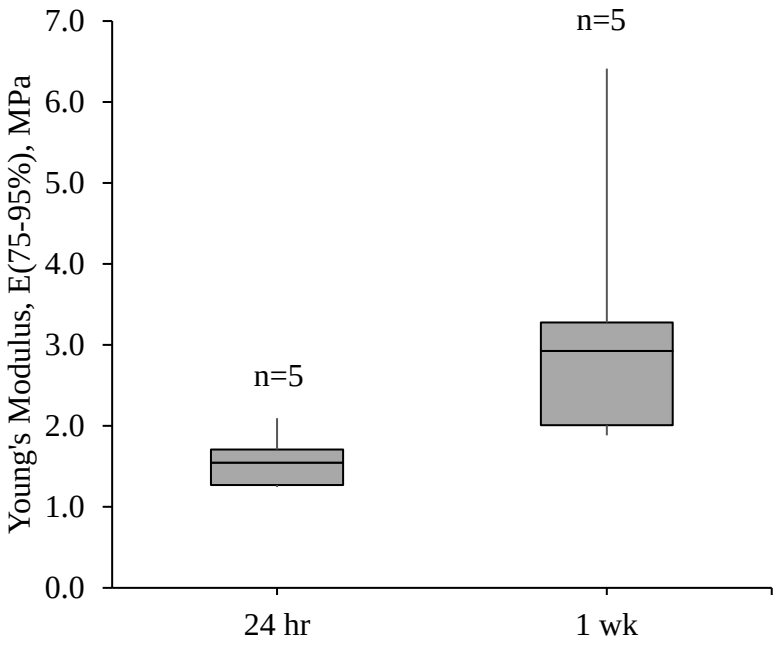

Figure 15. Boxplot of Young's modulus for strain range of 75-95% of emboli analogs formed at 50 RPM stored in PBS for 24 hours and 1 week (p=0.07).

3.2.2 *Dynamic vs. Static Environment*

Previous studies on the mechanical properties of pure fibrin clots offer insight to examining the compression testing data from the static and dynamic EAs. Typical compressive stress-strain plots of pure fibrin clots contain three regions including a linear elastic portion for $\varepsilon < 0.05\text{-}0.15$, an elastoplastic plateau until $\varepsilon = 0.3\text{-}0.5$, and non-linear stiffening of the clot for $\varepsilon > 0.5$ (Kim, 2014). The third region mentioned is described as strain hardening, which is common in biological gel-like structures (Weisel, 2017). Strain hardening is likely due to filaments resisting buckling under compression and increased fiber densification (Kim, 2014). In Figure 16, an example of the stress-strain curve for a pure fibrin clot from Kim et al. (2014) is compared with the resulting compression testing data for EAs formed at 50 RPM and 80 RPM, which

represent a low (1.45 MPa) and high (3.63 MPa) Young's modulus, respectively, for the two tissue segments. Graphs resulting in a higher Young's modulus are similar to the stress-strain curves exhibited by pure fibrin clots indicating composition may contribute to the mechanical strength of the EA.

A

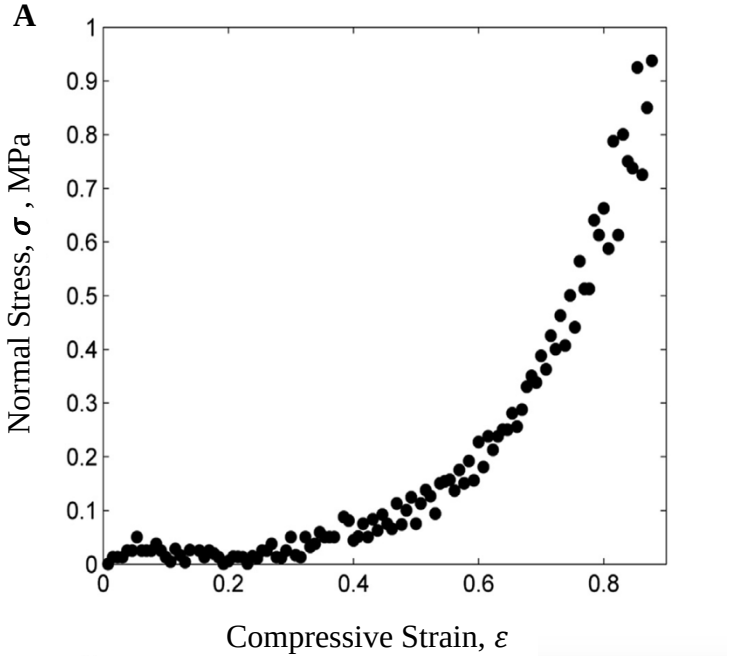
Normal Stress, σ , MPa
Compressive Strain, ε
0
0.1
0.2
0.3
0.4
0.5
0.6
0.7
0.8
0.9
1
0.2
0.4
0.6
0.8

B

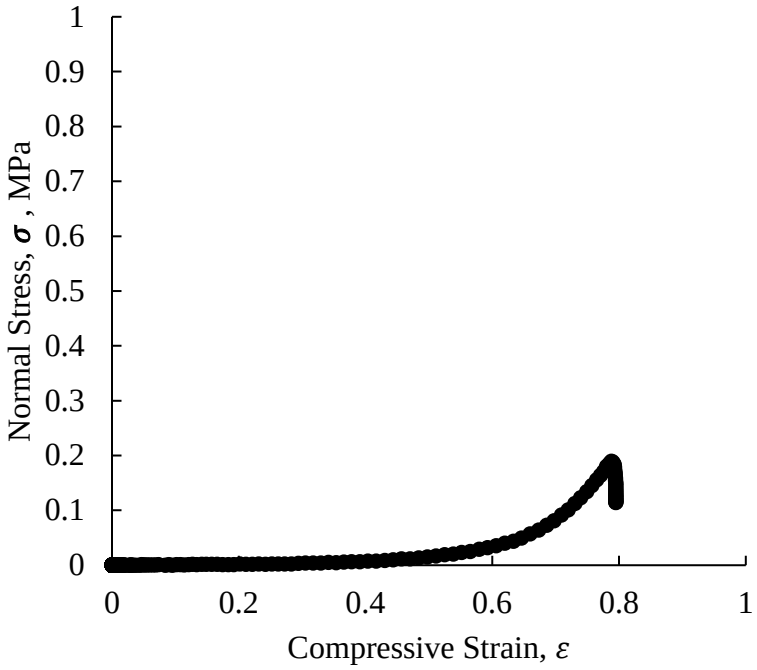
Normal Stress, σ , MPa
Compressive Strain, ε
0
0.1
0.2
0.3
0.4
0.5
0.6
0.7
0.8
0.9
1
0.2
0.4
0.6
0.8

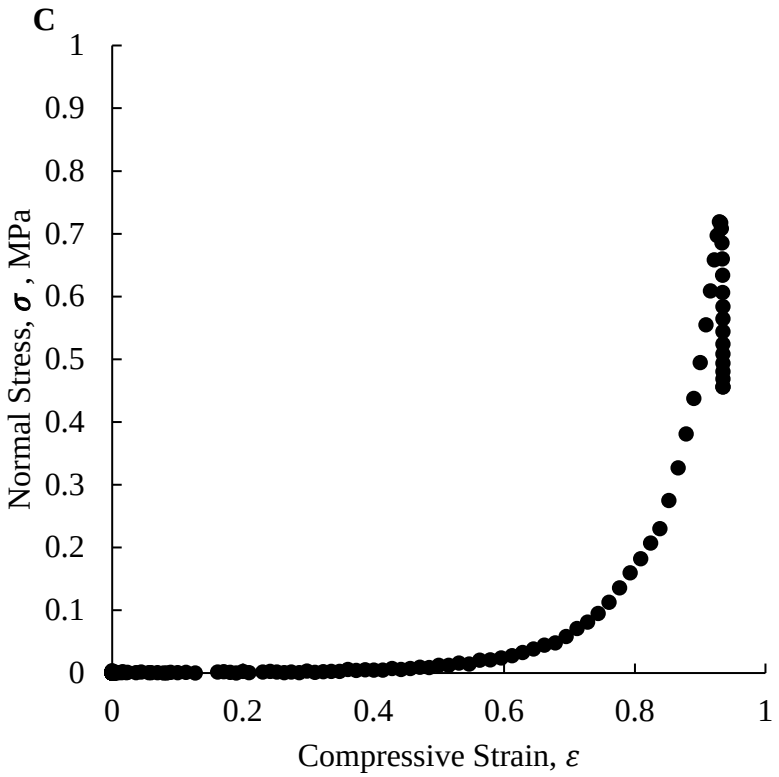

Figure 16. Normal stress, σ, vs. strain, ε, of (A) pure fibrin clots (O. V. Kim, Litvinov, Weisel, & Alber, 2014), and (B) dynamic EA formed at 50 RPM, and (C) dynamic EA formed at 80 RPM

The assumption of a purely elastic material, and therefore linear stress-strain relationship at 75-95% strain, proved true for a majority of the data. Average R^2 values were follows: 0.95 (0 RPM), 0.97 (34 RPM), 0.95 (50 RPM), and 0.97 (80 RPM). The lowest R^2 value overall was 0.87 in the mechanical testing data. This assumption was based on experiments conducted by Chueh et al. (2011) for the comparison of the proposed EAs to their findings on the material stiffness of thrombi.

Results from compression testing shown in Figure 17 exhibit a general upward trend of material stiffness with increasing flow rate. Young's modulus for the various environments are

compared with CEA thromboemboli in Table 1. Note that these values are reported as mean +/- SEM. Statistical analysis found a significant difference ($p<0.5$) between the static EAs and each of the dynamic EAs. In comparison with the CEA thromboemboli, the static EAs and dynamic EAs at 102 mL/min and 150 mL/min were not statistically significant.

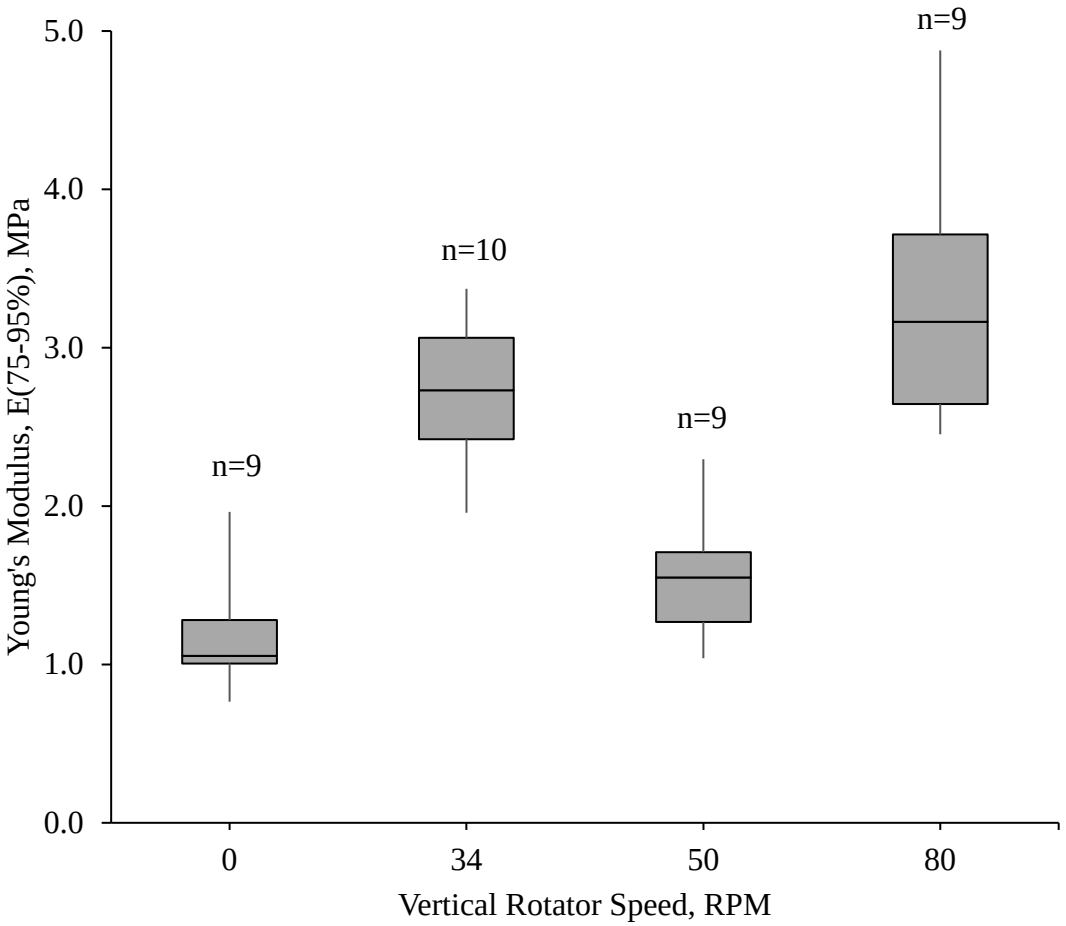

Figure 17. Boxplot of Young's modulus for strain range of 75-95% of static and dynamic emboli analogs (EA).

Table 1. Means and SEM of material stiffness comparison between static and dynamic emboli analogs and thromboemboli extracted from carotid endarterectomy (CEA). P-values for statistical significance with CEA Thromboemboli are also reported. *Value from Chueh et al. (2011)

	$E_{75-95\%}$ (MPa)	p-values
CEA Thromboemboli* (n=11)	1.60 +/- 0.50	
Static EA (n=9)	1.17 +/- 0.12	0.457
EA @ 34 RPM (n=10)	2.70 +/- 0.15	0.058
EA @ 50 RPM (n=9)	1.58 +/- 0.13	0.972
EA @ 80 RPM (n=9)	3.36 +/- 0.30	0.011

3.3 *Emboli Analog Physiological Properties*

Fibrin/platelets and RBCs of the dynamic EAs were analyzed through histology and image analysis as they are the primary components of thromboemboli. Images of the EAs are compared with previously published images of RBC-rich and fibrin-rich thrombi in Figure 18. Figure 18A shows a section of a RBC-rich thrombus whereas the section in Figure 18B is fibrin-rich. Although static EA tissue sections were difficult to obtain, several showed similarities in exhibiting loose connective fibrin on the perimeter of the EA and predominantly cherry-red or magenta stained RBCs in the middle as shown in Figure 18C. Figure 18D and Figure 18E are examples of tissue sections from EAs formed at 34 RPM and 50 RPM, respectively. Both samples show layers of light pink fibrin interspersed with individual RBCs as well as large and small clusters of RBCs. Figure 18F shows a fibrin-rich tissue section of an EA formed at 80 RPM. A few clusters of RBCs are scattered throughout the tissue sample as well as individual cells. Blue WBCs may be seen in all tissue samples.

As platelets cannot be distinguished from fibrin with H&E staining, they were reported together relative to RBCs in Figure 19. Further breakdown of compositions for each tissue section analyzed is summarized in Appendix B. Percent area of fibrin in the tissue sections for each dynamic environment are as follows: 63.29+/-13.00% (34 RPM), 67.84 +/- 21.40% (50 RPM) and 78.03 +/- 20.43% (80 RPM). Additionally, the percent areas of RBCs were: 36.71 +/- 13.00% (34 RPM), 32.16 +/-21.40% (50 RPM) and 21.97 +/- 20.43% (80 RPM). In comparison, Duffy et al. (2016) reported that the percent area of fibrin for their static EAs was 7.82 +/- 2.75%. Percent area of RBCs was 91.21 +/- 2.98% for their static EAs formed from sheep blood (Duffy et al., 2016).

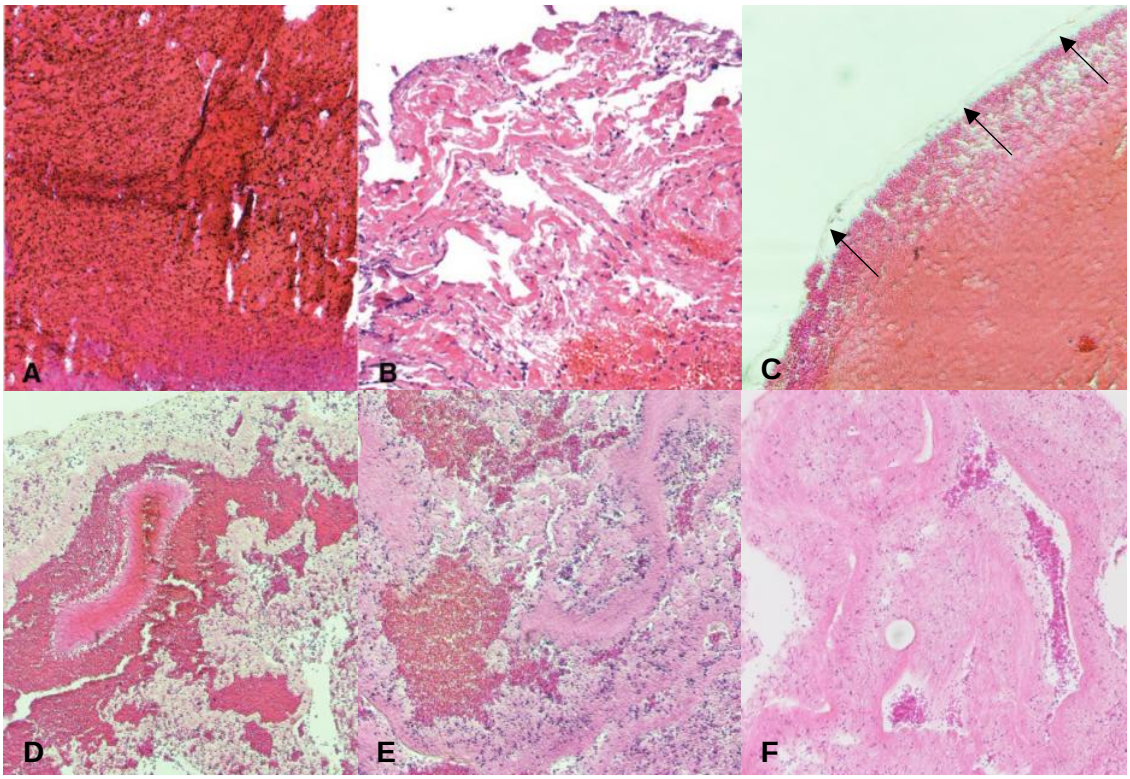

Figure 18. H&E staining of emboli analogs (EAs) created in four environments. A) RBC-rich thrombus (Liebeskind et al., 2011) B) Fibrin-rich thrombus (Liebeskind et al., 2011) C) Loose connective fibrin (arrows) located where RBC-rich clot formed against the tubing in a static environment (20X magnification). D) Vertical rotator speed equivalent to 34 RPM. EA is interspersed with RBCs in fibrin, platelets and leukocytes (10X magnification). E) EA formed at 50 RPM containing RBCs, fibrin, platelets and leukocytes (10X magnification). F) Vertical rotator speed was 80 RPM. EA contains some RBCs with primarily fibrin and platelets interspersed with leukocytes (10X magnification).

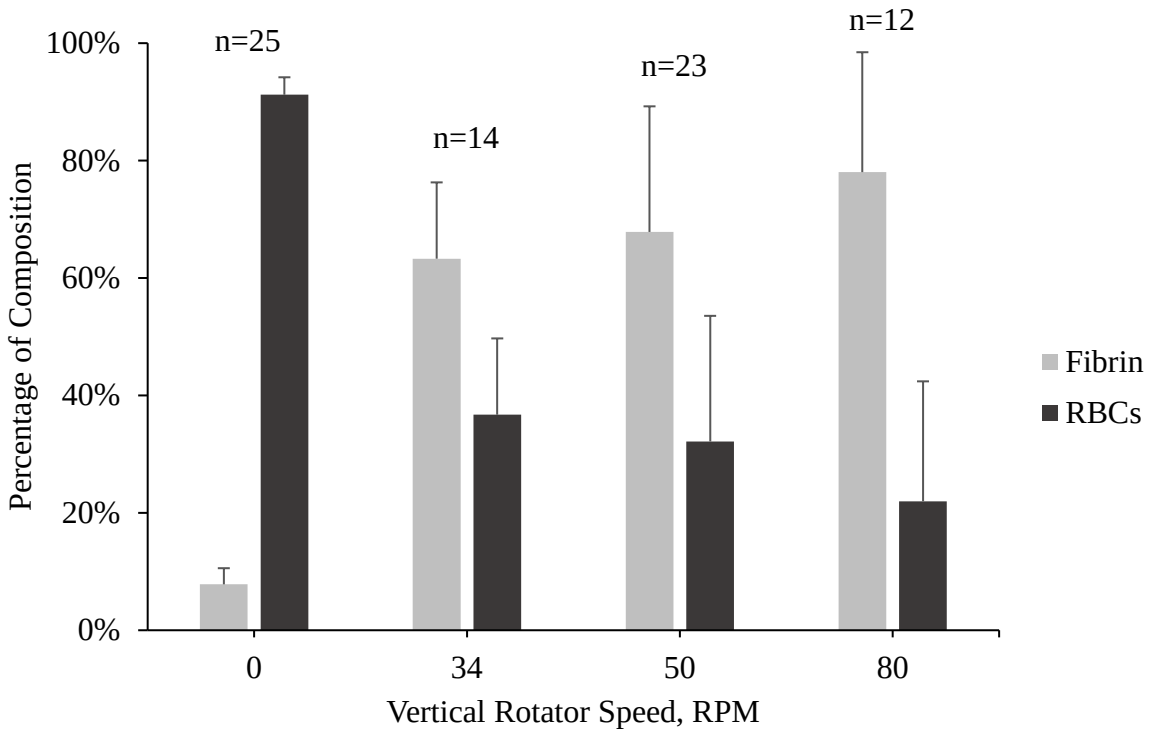

Figure 19. Trend of increasing amounts of fibrin/platelets and decreasing ratio of RBCs within the emboli analogs as a function of increasing volumetric flow rate. Note that data at 0 RPM is from Duffy et al. (2016).

3.4 *In-Vitro AIS Simulation Model*

3.4.1 *Temperature Regulation*

The desired physiological temperature of 37˚C (98.6 ˚F) was maintained during all experiments by adjustment of the water bath temperature. The temperature was set slightly higher (44˚C) than 37˚C to ensure that the inlet temperature of the vascular model would correspond to the body's natural temperature. The thermocouple thermometer measured and compared the water bath temperature and inlet temperature. Large fluctuations of the temperature were reduced after approximately one hour when steady-state conditions were reached and the temperature continued to slightly fluctuate within less than 2˚C.

3.4.2 *Flow Rate Analysis*

The desired flow range of 100-240 ml/min was achieved through pumping distilled water from a reservoir in the water bath to the system. The RPM on the peristaltic pump was altered to induce the flow rate and the corresponding output of the flow rate indicator was recorded. The flow rate was measured with a stopwatch and plastic beaker on a digital scale. Trials were repeated for a range of pump speed from 30 to 100 RPM. The RPM, volumetric flow rate and indicator value were recorded in a spreadsheet to create the following equations:

$$Q = 2.52 * RPM + 2.78 \qquad \text{Equation 4}$$

$$Q = 1113.5 * IV + 24.264 \qquad \text{Equation 5}$$

where Q is the volumetric flow rate (ml/min), RPM is the pump speed and IV is the indicator value from the digital flow rate indicator. These equations allow for the calculation of the system flow rate based on the pump speed as well as the output from the flow rate indicator. Both data sets fit the computed linear trendline well as the R^2 values were 0.99 and 0.99 for Equation 4 and Equation 5, respectively.

3.4.3 *Replication of Cerebral Arteries*

The first AIS vascular prototype was created with a confidential process. A primary complication from the initial prototype included bubbles forming in the silicone and hindering a clear view of the vessel conduit within the cured silicone model (Figure 20). After testing the model with an aspiration catheter Aspire RX-LP6 (Control Medical Technology, Hallandale, FL) one vessel angle was deemed too sharp to navigate the catheter through the conduit. A second iteration of the vascular model was prepared to reformat the connection between the model's

outlets and tubing, minimize bubbles within the silicone, alter the vessel angles, and include a bifurcation within the model.

Figure 20. First prototype of silicone vessel model

In the second iteration, the vessel was altered to have the ICA bifurcate into the MCA and BA. Although physiologically the BA does not attach to the ICA, this simplified the model to test a prototype in three vessels where stroke most commonly occurs. Note that this bifurcation does not follow Murray's Law for parent and daughter diameters in the following equation:

$$r_0{}^3 = r_1{}^3 + r_2{}^3 \qquad \text{Equation 6}$$

where r_0 is the radius of the ICA while r_1 and r_2 are the radii for the MCA and BA. Therefore, uniform shear stress within the network may not be assumed (Hoganson et al., 2010).

The vessel diameters were simplified to be 5 mm, 2.5 mm and 3 mm for the ICA, MCA and BA, respectively. This allowed for a direct connection of the vessel conduit to silicone tubing (Uxcell, Hong Kong) and eliminated the connection issue previously described in the first

iteration. These diameters were found to be within the physiological range for each vessel (Oktar et al., 2006; Smoker et al., 1986; Stock et al., 2000). Based on literature, the length of the ICA, MCA and BA were chosen to be 8.5 cm, 20 mm and 30 mm, respectively (Choudhry, Grantham, Rai, & Hogg, 2016; Pai, Varma, & Kulkarni, 2005; Zhang et al., 2014). Bubbles in the silicone were eliminated by degassing the silicone in a vacuum pressure chamber immediately after mixing but prior to pouring. Several bubbles formed on the sides of the acrylic box and top surface exposed to the air during the curing process; however, the bottom of the mold was completely clear as seen in Figure 21. The sharpest vessel angle was changed to 74.4º, which is the mean angle of cerebral vasculature (Canham & Finlay, 2004).

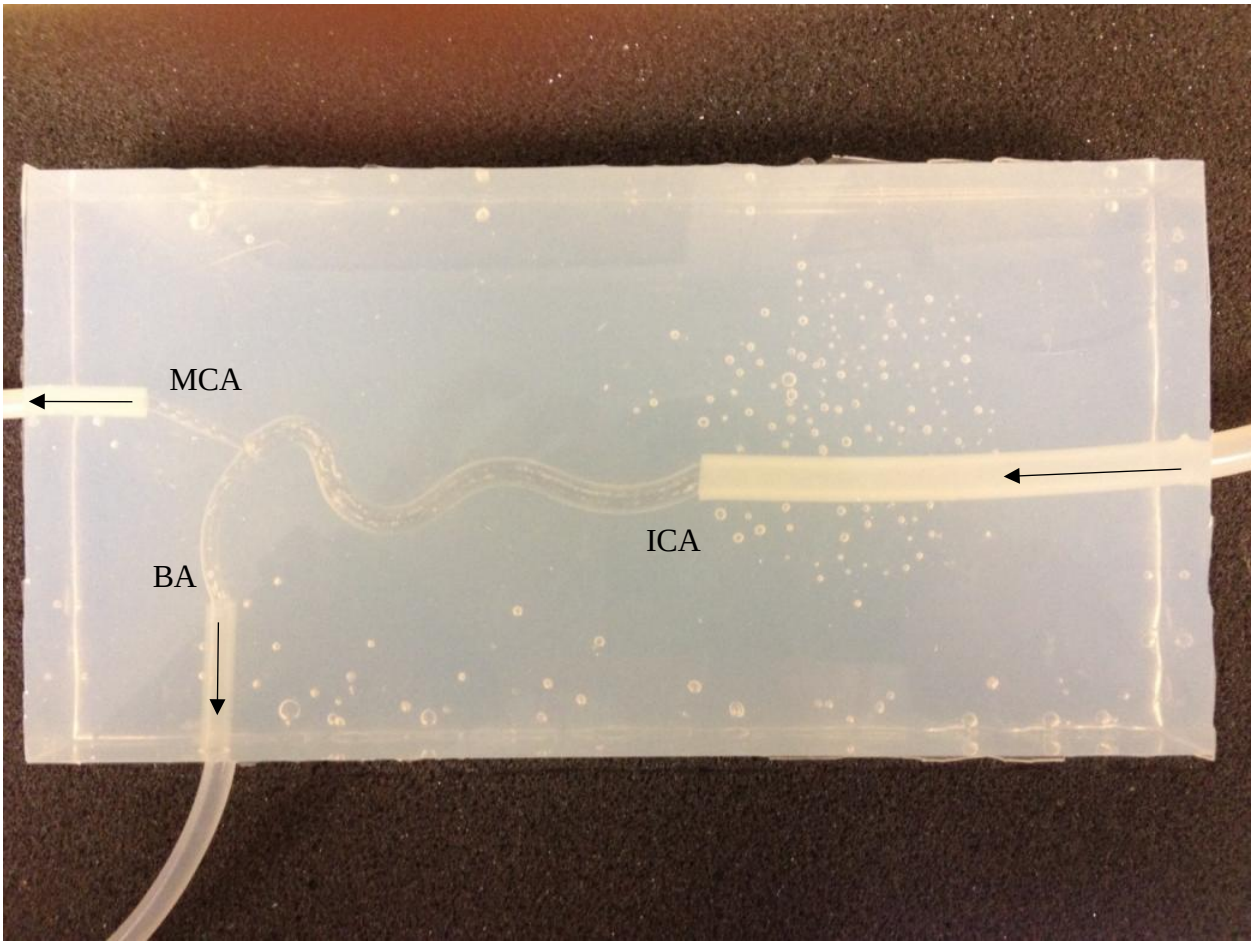

Figure 21. Second prototype of silicone vessel model

4 Discussion

4.1 *Emboli Analog Dimensions*

Blood volume and tubing width were optimized with the dynamic system to produce EAs with similar dimensions of stroke thromboemboli retrieved from the ICA. Although statically formed EAs were longer, the blood volume could be adjusted to obtain statically formed EAs with dimensions resembling stroke emboli as well. Blood volume and tubing width could also be altered to obtain EAs mimicking dimensions of thromboemboli from other vessels. For direct comparison of material stiffness and composition between the static and dynamic environments, all parameters excluding the induced volumetric flow rate remained the same. With the proposed method, EAs can be easily formed in a dynamic system to resemble dimensions of stroke emboli extracted from the ICA.

4.2 *Emboli Analog Material Stiffness*

4.2.1 *Storage Conditions*

As storage conditions were not statistically significant (p=0.07), EAs stored in PBS for one week could be used for prototype testing. However, the material stiffness of the EAs stored for one week exhibited large variations reflected in the high standard deviation. The average $E_{75-95\%}$ for one EA was 6.41 MPa, which is four times the average $E_{75-95\%}$ of retrieved thromboemboli from CEA procedures (Chueh et al., 2011). Unpredictability of the EA material stiffness during prototype testing may skew results, and therefore EAs are not recommended to be stored in PBS for one week.

4.2.2 *Emboli Analogs vs. Human Stroke Thromboemboli*

Approximately 11% of the tissue segments analyzed exhibited non-linear deformation after an initial yield point. In addition to the date shown in Figure 22, stress-strain curves with the same non-linearity are also shown in Appendix C. Over 60% of those tissue segments were from statically formed EAs, suggesting that the composition of the EAs contributed to the non-linearity.

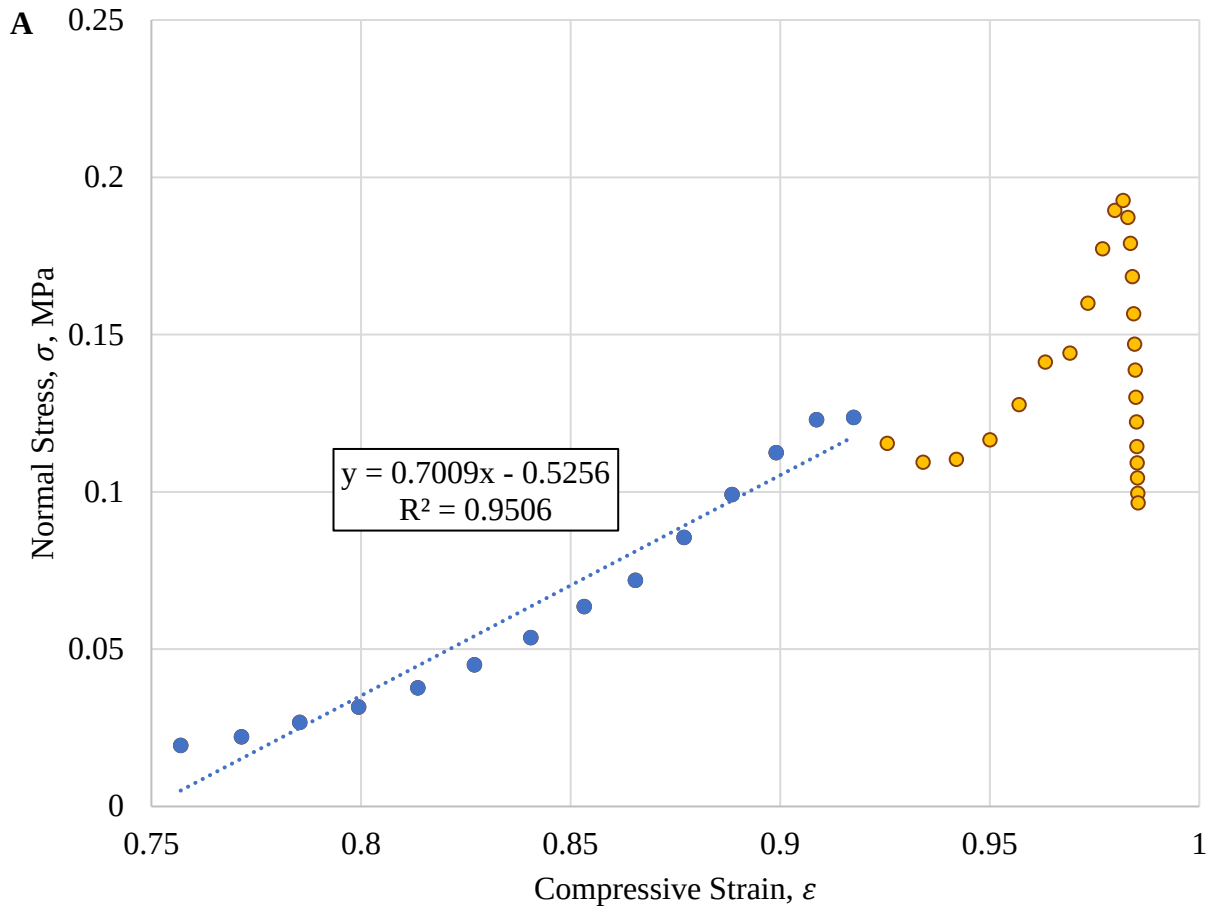

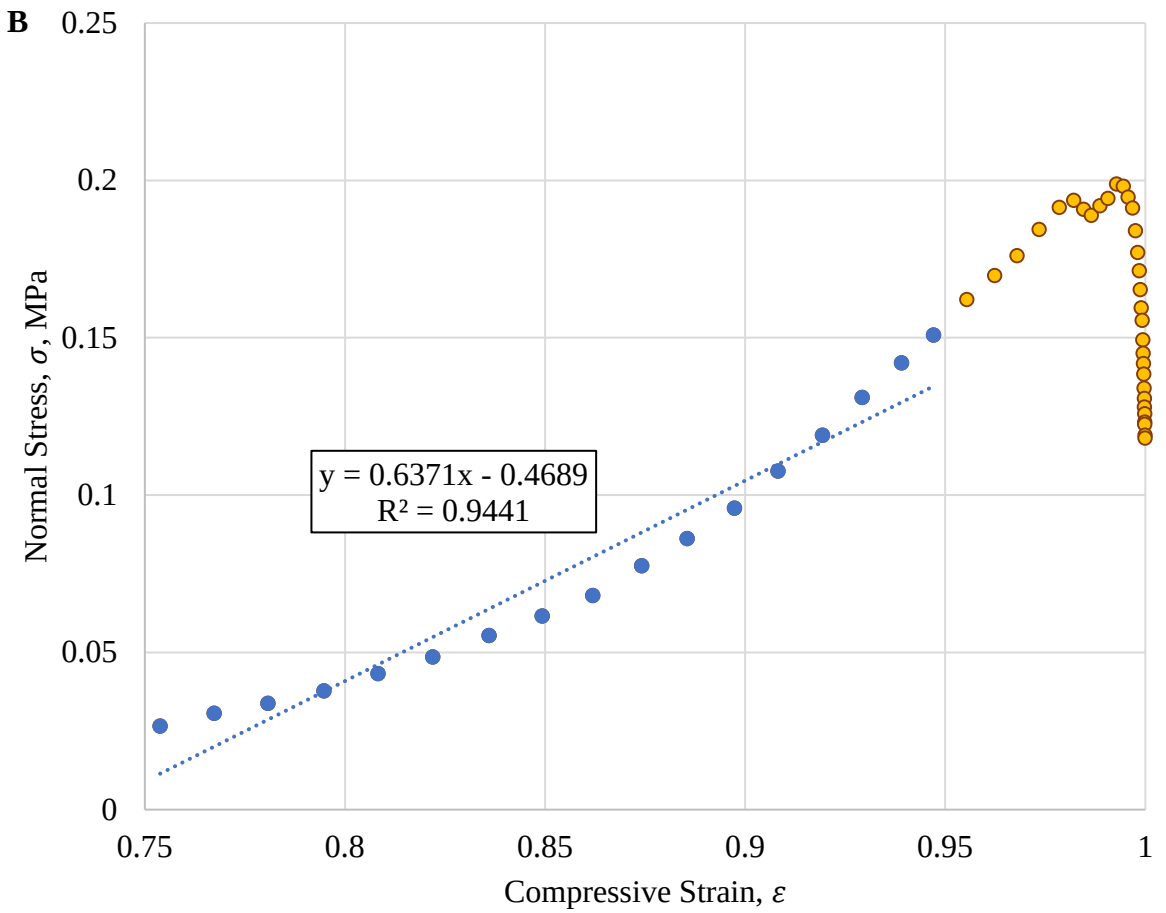

Figure 22. Normal stress, σ, versus compressive strain, ε, of A) static EA and B) dynamic EA (50 RPM) demonstrate non-linearity after initial yield point followed by continued strain hardening of the fibrin in each EA. Young's modulus is calculated for data points from 75% strain until 95% strain or initial yield point is reached.

In Figure 22, the initial yield point may be due to failing of the mechanical strength of RBCs, whereas the fibrin-platelet network continues strain hardening until permanent deformation occurs. Individual fibrin fibers have been found to unfold from their typical coiled-coil structure to become β-sheets under compression (Weisel, 2017; Kim, 2014). One analogy to describe the stress-strain relationship exhibited may be water balloons (RBCs) intertwined with a spring (fibrin). Once the balloon or cell membranes break, the spring will continue to deform under the applied load until it experiences permanent deformation. As this phenomenon was

found most frequently in static EAs, it is most likely composition dependent. The dynamic EAs that exhibited similar behavior may be due to a higher percentage of RBCs within the specific sample tested. In Figure 14A of the example dynamic EA, a small red portion may be inferred as RBC-rich whereas the rest of the sample within view is predominantly fibrin.

Stress-strain curves of the dynamic EAs revealed a brief decrease in strain for a short strain range versus stress-strain curves of static EAs that decreased and then began strain hardening for a longer strain range. This also points towards the described phenomenon being composition dependent as the static EAs had a higher percentage of RBCs than the dynamic EAs.

The dynamic method discussed demonstrates the ability to offer EAs with a range of compositions and mechanical properties for prototype testing. Table 1 reveals that porcine emboli formed at 50 RPM exhibit mechanical properties nearly identical to thromboemboli extracted from CEA ($p=0.972$). These thromboemboli were described as highly inhomogeneous; however, exact compositions were not documented (Chueh et al., 2011). Fibrin-rich clots have been identified as a cause for recanalization issues (Hashimoto et al., 2016; Yuki et al., 2012). Therefore, the dynamic process at 50 RPM should be used to produce EAs that are fibrin-rich and mimic the material stiffness of human stroke thromboemboli.

4.3 *Emboli Analog Physiological Properties*

4.3.1 *Emboli Analogs vs. Human Stroke Thromboemboli*

Chueh et al. (2011) discussed the need to create an emboli analog model to test and modify endovascular recanalization devices as the mechanical properties of the model will determine the device performance. The emboli analogs developed from human, porcine and bovine blood were composed of primarily RBCs surrounded by a thin outer layer of fibrin where the emboli analog

had developed against the tubing. Similarly, our static EAs also exhibited a thin band of fibrin circulating the RBCs where the EA had been in contact with the tubing. Arrows in Figure 18C point to loose connective fibrin at the edge of the tissue section. Although Chueh et al. (2011) created emboli analogs similar in material stiffness to the human stroke thromboemboli, the histological findings concur that simply adding various concentrations of thrombin, blood and coagulant will result in a homogeneous EA. Nearly 70% of thromboemboli retrieved in three clinical studies were described as having a serpentine or layered pattern of fibrin, RBCs, platelets and WBCs (Cline et al., 2013; Marder et al., 2006; Schuhmann et al., 2016). Similar patterns are achieved in the dynamically formed EAs as seen in Figure 18.

4.3.2 *Material Stiffness vs. Composition Results*

While the histology results appear to be conclusive that increasing flow rates result in increasing amounts of fibrin/platelets and an inverse relationship with RBCs, the results do not correspond with the discrepancy between the material stiffness results. For example, at 34 RPM the material stiffness was higher than at 50 RPM. One explanation may be the fibrin morphology differences as one study found that maximum clot stiffness correlated with thick fibers and highly branched fibrin (Ryan, Mockros, Weisel, & Lorand, 1999). The authors note that fiber thickness and branching are inversely related; therefore, these two parameters must be in "equilibrium" to exhibit maximum clot stiffness. This may be plausible for EAs formed at 34 RPM as the RBCs generally were found in clusters, which would allow thicker fibers to form around the RBC clusters. Additionally, RBCs scattered within the fibrin may encourage branching of the fibrin network. Distribution of RBCs may point to how fibrin fibers form within

the EAs, which may be examined through images from a scanning electron microscope (SEM) to indicate fiber alignment, diameter as well as RBC distribution.

Distribution of RBCs within the fibrin network may also contribute to differences in material stiffness. One study found that platelet and fibrin concentrations influence RBCs contracting to a polyhedral formation, aptly named polyhedrocytes (Cines et al., 2014). As the polyhedral structure results in an efficient, tight-packing of RBCs, material stiffness of these clots would be higher than EAs with RBCs evenly distributed within the fibrin network. Additionally, Cines et al. (2014) observed erythrocytes excluded during clot formation, which they hypothesized was due to platelet contraction initiating clusters of polyhedrocytes and simultaneously forcing some erythrocytes from the fibrin network. This concurs with our findings that at higher blood flow rates, and therefore higher external forces, more platelets and fibrin formed while the percentage of RBCs was low. SEM may provide a deeper insight to the differences in the material stiffness of EAs formed at 34 RPM and 50 RPM.

4.4 *In-Vitro AIS Simulation Model*

Temperature regulation of the in-vitro AIS simulation model was successfully achieved to obtain the physiological temperature of 37 ºC. The pump speed, flow rate indicator value and volumetric flow rate were correlated to produce two equations. This allows the user to input a specific pump speed for the desired flow rate and compare with the output from the flow rate indicator. From a separate trial, the error between the two equations was calculated to be 0.16% from a pump speed of 70 RPM and indicator value of 0.139. To obtain an inlet flow rate of 240 mL/min corresponding to the ICA, a pump speed of 94 RPM is recommended. This setting should produce an indicator value of 0.193 for the desired flow rate.

Two iterations of the silicone vascular model provided a final model with dimensions similar to the ICA, MCA and BA in terms of their diameter, length and tortuosity. As ABS is a common material in additive manufacturing, the majority of 3D printing equipment should be able to replicate any desired vasculature for research purposes. Clear visibility of the vessel allows for a camera to capture embolization and removal during prototype testing. This mold provides a platform that may be easily altered to explore alternative cerebral vasculature for stroke research.

4.5 *Limitations*

Image size of the tissue sections remains one limitation for the composition analysis used for this research. Future adjustments for the MATLAB code could include breaking the images into smaller segments to increase the number of pixels for each total image examined by the MATLAB code and therefore, increase threshold sensitivity. Other limitations include a small sample size (n) for the composition analysis and material stiffness data. One method of storage was explored, yet other methods may provide appropriate conditions for storage of EAs long-term. Also, the volumetric blood flow rate is relative to low, medium and high speeds rather than exact flow rates. This is due to a small portion of the blood thinning out along the tubing wall.

5 Future Directions

Further analysis of EA material stiffness and composition analysis include additional staining methods and SEM. Platelets and fibrin were calculated together, yet platelets could be separated using immunohistochemistry staining methods to identify exact compositions of platelets, fibrin and RBCs. Alternative staining methods to examine fibrin/platelets and RBCs

include Martius, Scarlet and Blue (MSB). Previous research has found no significant difference between H&E and MSB staining methods for identifying the content percentage of RBCs, fibrin/platelets and WBCs (Duffy et al., 2016). Another component to examine may be atheromateous gruel, which is cholesterol clefts or foam cells. Of 251 patients examined for atheromatous gruel, 11 (4.4%) thromboemboli were positive (Chueh et al., 2011; Hashimoto et al., 2016; S. K. Kim et al., 2015; Krajíčková et al., 2017; Marder et al., 2006; Niesten et al., 2014). WBCs may be another component of the EAs to examine as cardioembolic thrombi have more WBCs than noncardioembolic thrombi (Sporns et al., 2017). Material stiffness of EAs could be further examined with SEM to indicate the microstructure and investigate fibrin fiber alignment, fiber diameter and RBC distribution. Thus, clot etiology may be further explored through identifying multiple components of EAs and comparing with human stroke thromboemboli.

Using advances in imaging modalities, researchers are linking clot composition with imaging artifacts (Liebeskind et al., 2011; Simons et al., 2015). Liebeskind et al. (2011) examined the link between CT and MRI imaging markers with pathology of thrombi obtained from human stroke patients. Specific imaging features included hyperdense middle cerebral artery sign on CT and gradient-echo blooming artifact on MRI. Simons et al. (2014) also examined the CT imaging feature hyperdense artery sign (HAS) for comparison with thrombus composition. They used CD34 to identify endothelial cells in thrombi. If positively identified, the endothelial cells demonstrated that the sample was a late phase organized fibrin thrombus. HAS was found more frequently in early phase thrombi (65.5%) versus late phase thrombi (34.5%) (Simons et al., 2015). From this knowledge, one may be able to know the type of stroke clot and adapt the retrieval mechanism to the clot composition. With the proposed methodology of fibrin-

rich EA formation, continued research on retrieval mechanisms specific to fibrin-rich thromboemboli may be explored.

Regarding the in-vitro model to simulate AIS, temperature and flow rate data collection could be automated with LABVIEW. This would allow for a feedback control loop to ensure that the temperature and flow rate remain constant during prototype testing of a retrieval mechanism. Distilled water in the flow loop may be replaced by a 40% (w/v) glycerin solution to obtain a fluid viscosity similar to blood. Additionally, ballistics gel is an alternative material to silicone in the vascular model as it is known to effectively mimic human tissue properties.

6 Conclusions

Conditions used to create EAs have a significant impact on their composition and mechanical properties. Static conditions will yield a comparable material stiffness to cerebral thromboemboli, yet will be primarily composed of RBCs with a thin network of fibrin surrounding the EA. Dynamic conditions may be altered to obtain EAs mimicking material stiffness of CEA thromboemboli and compositions of varying percentages of fibrin, platelets and RBCs. Specifically, the EAs formed at 50 RPM were found to be nearly identical in their material stiffness with CEA thromboemboli ($p=0.972$). Long-term storage of EAs in PBS for one week is not recommended due to the high variability in material stiffness of EAs stored for 1 week at 4°C. Testing of stroke retrieval mechanisms should be conducted with EAs that have well-defined and validated characteristics that make them appropriate to represent human stroke thromboemboli.

Through this project, a new method to replicate brain vasculature tortuosity and inner diameters of the arteries has been developed. This system will ensure that the retrieval device

could move realistically in human brain vasculature to extract a stroke clot. The described in-vitro model is essential to simulate AIS parameters and test prototypes of a mechanism for clot retrieval in stroke patients.

References

American Heart Association (2015). let's talk about Ischemic Stroke. Retrieved from http://www.strokeassociation.org/idc/groups/stroke-public/@wcm/@hcm/documents/downloadable/ucm_309725.pdf

American Heart Association (2016). Types of Stroke. Retrieved from http://www.strokeassociation.org/STROKEORG/AboutStroke/TypesofStroke/Types-of-Stroke_UCM_308531_SubHomePage.jsp

Behme, D., Gondecki, L., Fiethen, S., Kowoll, A., Mpotsaris, A., & Weber, W. (2014). Complications of mechanical thrombectomy for acute ischemic stroke-a retrospective single-center study of 176 consecutive cases. *Neuroradiology, 56*(6), 467-476. doi:10.1007/s00234-014-1352-0

Boeckh-Behrens, T., Kleine, J. F., Zimmer, C., Neff, F., Scheipl, F., Pelisek, J., . . . Poppert, H. (2016). Thrombus Histology Suggests Cardioembolic Cause in Cryptogenic Stroke. *Stroke, 47*(7), 1864-1871. doi:10.1161/STROKEAHA.116.013105

Canham, P. B., & Finlay, H. M. (2004). Morphometry of medial gaps of human brain artery branches. *Stroke, 35*(5), 1153-1157. doi:10.1161/01.STR.0000124926.76836.df

Choudhry, F. A., Grantham, J. T., Rai, A. T., & Hogg, J. P. (2016). Vascular geometry of the extracranial carotid arteries: an analysis of length, diameter, and tortuosity. *J Neurointerv Surg, 8*(5), 536-540. doi:10.1136/neurintsurg-2015-011671

Chueh, J. Y., Wakhloo, A. K., & Gounis, M. J. (2009). Neurovascular modeling: small-batch manufacturing of silicone vascular replicas. *AJNR Am J Neuroradiol, 30*(6), 1159-1164. doi:10.3174/ajnr.A1543

Chueh, J. Y., Wakhloo, A. K., Hendricks, G. H., Silva, C. F., Weaver, J. P., & Gounis, M. J. (2011). Mechanical characterization of thromboemboli in acute ischemic stroke and laboratory embolus analogs. *AJNR Am J Neuroradiol, 32*(7), 1237-1244. doi:10.3174/ajnr.A2485

Cines, D. B., Lebedeva, T., Nagaswami, C., Hayes, V., Massefski, W., Litvinov, R. I., . . . Weisel, J. W. (2014). Clot contraction: compression of erythrocytes into tightly packed polyhedra and redistribution of platelets and fibrin. *Blood, 123*(10), 1596-1603. doi:10.1182/blood-2013-08-523860

Cline, B., Carpenter, J., & Rai, A. (2013). *O-027 Pathological Analysis of Extracted Clots in Embolectomy Patients with Acute Ischaemic Stroke.* Paper presented at the SNIS 10th Annual Meeting, Journal of NeuroInterventional Surgery.

Duffy, S., Farrell, M., McArdle, K., Thornton, J., Vale, D., Rainsford, E., . . . Gilvarry, M. (2016). Novel methodology to replicate clot analogs with diverse composition in acute ischemic stroke. *J Neurointerv Surg*. doi:10.1136/neurintsurg-2016-012308

Fogelson, A. L., & Neeves, K. B. (2015). Fluid Mechanics of Blood Clot Formation. *Annu Rev Fluid Mech, 47*, 377-403. doi:10.1146/annurev-fluid-010814-014513

Gascou, G., Lobotesis, K., Machi, P., Maldonado, I., Vendrell, J. F., Riquelme, C., . . . Costalat, V. (2014). Stent retrievers in acute ischemic stroke: complications and failures during the perioperative period. *AJNR Am J Neuroradiol, 35*(4), 734-740. doi:10.3174/ajnr.A3746

Hashimoto, T., Hayakawa, M., Funatsu, N., Yamagami, H., Satow, T., Takahashi, J. C., . . . Toyoda, K. (2016). Histopathologic Analysis of Retrieved Thrombi Associated With Successful Reperfusion After Acute Stroke Thrombectomy. *Stroke, 47*(12), 3035-3037. doi:10.1161/STROKEAHA.116.015228

Hoganson, D. M., Pryor, H. I., Spool, I. D., Burns, O. H., Gilmore, J. R., & Vacanti, J. P. (2010). Principles of biomimetic vascular network design applied to a tissue-engineered liver scaffold. *Tissue Eng Part A, 16*(5), 1469-1477. doi:10.1089/ten.TEA.2009.0118

Ionita, C. N., Mokin, M., Varble, N., Bednarek, D. R., Xiang, J., Snyder, K. V., . . . Rudin, S. (2014). Challenges and limitations of patient-specific vascular phantom fabrication using 3D Polyjet printing. *Proc SPIE Int Soc Opt Eng, 9038*, 90380M. doi:10.1117/12.2042266

Kan, I., Yuki, I., Murayama, Y., Vi ñ uela, F. A., Kim, R. H., Vinter, H. V., & Vi ñ uela, F. (2010). A Novel Method of Thrombus Preparation for Use in a Swine Model for Evaluation of Thrombectomy Devices. *American Journal of Neuroradiology, 31*, 1741-1743.

Kandel, E. R., Schwartz, J. H., & Jessell, T. M. (2000). *Principles of neural science* (4th ed.). New York: McGraw-Hill, Health Professions Division.

Khan, A. M. (2015). Stain Normalization Toolbox. Retrieved from https://warwick.ac.uk/fac/sci/dcs/research/tia/software/sntoolbox/

Kim, O. V., Litvinov, R. I., Weisel, J. W., & Alber, M. S. (2014). Structural basis for the nonlinear mechanics of fibrin networks under compression. *Biomaterials, 35*(25), 6739-6749. doi:10.1016/j.biomaterials.2014.04.056

Kim, S. K., Yoon, W., Kim, T. S., Kim, H. S., Heo, T. W., & Park, M. S. (2015). Histologic Analysis of Retrieved Clots in Acute Ischemic Stroke: Correlation with Stroke Etiology and Gradient-Echo MRI. *AJNR Am J Neuroradiol, 36*(9), 1756-1762. doi:10.3174/ajnr.A4402

Knox, K., Kerber, C. W., Singel, S. A., Bailey, M. J., & Imbesi, S. G. (2005). Rapid prototyping to create vascular replicas from CT scan data: making tools to teach, rehearse, and choose treatment strategies. *Catheter Cardiovasc Interv, 65*(1), 47-53. doi:10.1002/ccd.20333

Krajíčková, D., Krajina, A., Šteiner, I., Vyšata, O., Herzig, R., Lojík, M., . . . Vališ, M. (2017). Fibrin Clot Architecture in Acute Ischemic Stroke Treated With Mechanical Thrombectomy With Stent-Retrievers - Cohort Study. *Circ J*. doi:10.1253/circj.CJ-17-0375

Kurre, W., Vorlaender, K., Aguilar-Pérez, M., Schmid, E., Bäzner, H., & Henkes, H. (2013). Frequency and relevance of anterior cerebral artery embolism caused by mechanical thrombectomy of middle cerebral artery occlusion. *AJNR Am J Neuroradiol, 34*(8), 1606-1611. doi:10.3174/ajnr.A3462

Liebeskind, D. S., Sanossian, N., Yong, W. H., Starkman, S., Tsang, M. P., Moya, A. L., . . . Saver, J. L. (2011). CT and MRI early vessel signs reflect clot composition in acute stroke. *Stroke, 42*(5), 1237-1243. doi:10.1161/STROKEAHA.110.605576

Macenko, M., Niethammer, M., Marron, J. S., Borland, D., Woosley, J. T., Guan, X., . . . Thomas, N. E. (2009). *A Method for Normalizing Histology Slides for Quantitative Analysis*. Paper presented at the IEEE International Symposium on Biomedical Imaging.

Marder, V. J., Chute, D. J., Starkman, S., Abolian, A. M., Kidwell, C., Liebeskind, D., . . . Saver, J. L. (2006). Analysis of thrombi retrieved from cerebral arteries of patients with acute ischemic stroke. *Stroke, 37*(8), 2086-2093. doi:10.1161/01.STR.0000230307.03438.94

Mokin, M., Fargen, K. M., Primiani, C. T., Ren, Z., Dumont, T. M., Brasiliense, L. B., . . . Siddiqui, A. H. (2016). Vessel perforation during stent retriever thrombectomy for acute ischemic stroke: technical details and clinical outcomes. *J Neurointerv Surg*. doi:10.1136/neurintsurg-2016-012707

Mokin, M., Setlur Nagesh, S. V., Ionita, C. N., Mocco, J., & Siddiqui, A. H. (2016). Stent retriever thrombectomy with the Cover accessory device versus proximal protection with a balloon guide catheter: in vitro stroke model comparison. *J Neurointerv Surg, 8*(4), 413-417. doi:10.1136/neurintsurg-2014-011617

Mozaffarian, D., Benjamin, E. J., Go, A. S., Arnett, D. K., Blaha, M. J., Cushman, M., . . . Subcommittee, S. S. (2016). Heart Disease and Stroke Statistics-2016 Update: A Report From the American Heart Association. *Circulation, 133*(4), e38-360. doi:10.1161/CIR.0000000000000350

Niesten, J. M., van der Schaaf, I. C., van Dam, L., Vink, A., Vos, J. A., Schonewille, W. J., . . . Velthuis, B. K. (2014). Histopathologic composition of cerebral thrombi of acute stroke patients is correlated with stroke subtype and thrombus attenuation. *PLoS One, 9*(2), e88882. doi:10.1371/journal.pone.0088882

Oktar, S. O., Yücel, C., Karaosmanoglu, D., Akkan, K., Ozdemir, H., Tokgoz, N., & Tali, T. (2006). Blood-flow volume quantification in internal carotid and vertebral arteries: comparison of 3 different ultrasound techniques with phase-contrast MR imaging. *AJNR Am J Neuroradiol, 27*(2), 363-369.

Onasoga-Jarvis, A. A., Puls, T. J., O'Brien, S. K., Kuang, L., Liang, H. J., & Neeves, K. B. (2014). Thrombin generation and fibrin formation under flow on biomimetic tissue factor-rich surfaces. *International Society on Thrombosis and Haemostasis, 12*, 373-382.

Pai, S. B., Varma, R. G., & Kulkarni, R. N. (2005). Microsurgical anatomy of the middle cerebral artery. *Neurol India, 53*(2), 186-190.

Paramasivam, S. (2015). Current trends in the management of acute ischemic stroke. *Neurol India, 63*(5), 665-672. doi:10.4103/0028-3886.166547

Ruifrok, A. C., & Johnston, D. A. (2001). Quantification of histological staining by color deconvolution. *Anal Quant Cytol Histol 23*(4), 291-299.

Ryan, E. A., Mockros, L. F., Weisel, J. W., & Lorand, L. (1999). Structural origins of fibrin clot rheology. *Biophys J, 77*(5), 2813-2826. doi:10.1016/S0006-3495(99)77113-4

Schuhmann, M. K., Gunreben, I., Kleinschnitz, C., & Kraft, P. (2016). Immunohistochemical Analysis of Cerebral Thrombi Retrieved by Mechanical Thrombectomy from Patients with Acute Ischemic Stroke. *Int J Mol Sci, 17*(3), 298. doi:10.3390/ijms17030298

Seong, J., Sadasivan, C., Onizuka, M., Gounis, M. J., Christian, F., Miskolczi, L., . . . Lieber, B. B. (2005). Morphology of elastase-induced cerebral aneurysm model in rabbit and rapid prototyping of elastomeric transparent replicas. *Biorheology, 42*(5), 345-361.

Simons, N., Mitchell, P., Dowling, R., Gonzales, M., & Yan, B. (2015). Thrombus composition in acute ischemic stroke: a histopathological study of thrombus extracted by endovascular retrieval. *J Neuroradiol, 42*(2), 86-92. doi:10.1016/j.neurad.2014.01.124

Smoker, W. R., Price, M. J., Keyes, W. D., Corbett, J. J., & Gentry, L. R. (1986). High-resolution computed tomography of the basilar artery: 1. Normal size and position. *AJNR Am J Neuroradiol, 7*(1), 55-60.

Sporns, P. B., Hanning, U., Schwindt, W., Velasco, A., Minnerup, J., Zoubi, T., . . . Niederstadt, T. U. (2017). Ischemic Stroke: What Does the Histological Composition Tell Us About the Origin of the Thrombus? *Stroke, 48*(8), 2206-2210 doi:10.1161/STROKEAHA.117.016590

Stock, K. W., Wetzel, S. G., Lyrer, P. A., & Radü, E. W. (2000). Quantification of blood flow in the middle cerebral artery with phase-contrast MR imaging. *Eur Radiol, 10*(11), 1795-1800. doi:10.1007/s003300000378

Sugiu, K., Martin, J. B., Jean, B., Gailloud, P., Mandai, S., & Rufenacht, D. A. (2003). Artificial cerebral aneurysm model for medical testing, training, and research. *Neurol Med Chir (Tokyo), 43*(2), 69-72; discussion 73.

Tomkins, A. J., Schleicher, N., Murtha, L., Kaps, M., Levi, C. R., Nedelmann, M., & Spratt, N. J. (2015). Platelet rich clots are resistant to lysis by thrombolytic therapy in a rat model of embolic stroke. *Exp Transl Stroke Med, 7*, 2. doi:10.1186/s13231-014-0014-y

Veta, M. (2015). Staining-normalization. Retrieved from https://github.com/mitkovetta/staining-normalization/blob/master/normalizeStaining.m

Weisel, J. W., & Litvinov, R. I. (2017). Fibrin Formation, Structure and Properties. *Subcell Biochem, 82*, 405-456. doi:10.1007/978-3-319-49674-0_13

Wetzel, S. G., Ohta, M., Handa, A., Auer, J. M., Lylyk, P., Lovblad, K. O., . . . Rufenacht, D. A. (2005). From patient to model: stereolithographic modeling of the cerebral vasculature based on rotational angiography. *AJNR Am J Neuroradiol, 26*(6), 1425-1427.

Yuki, I., Kan, I., Vinters, H. V., Kim, R. H., Golshan, A., Vinuela, F. A., . . . Vinuela, F. (2012). The impact of thromboemboli histology on the performance of a mechanical thrombectomy device. *AJNR Am J Neuroradiol, 33*(4), 643-648. doi:10.3174/ajnr.A2842

Zhang, D. P., Zhang, S. L., Zhang, J. W., Zhang, H. T., Fu, S. Q., Yu, M., . . . Ji, P. (2014). Basilar artery bending length, vascular risk factors, and pontine infarction. *J Neurol Sci, 338*(1-2), 142-147. doi:10.1016/j.jns.2013.12.037

Appendix A: Automated Histology Analysis

```
%Goal: Automate the analysis of H&E stained sections of emboli analogs to
%determine the percentage of fibrin to red blood cells (RBCs) in the sample.
%(1) Perform normalization and color deconvolution of the histology images
%(2) Obtain Eosin stained image and compare percentage of fibrin to erythrocytes (RBCs)

%% References-----------------------------------------------------------------------------------------
%Khan,  A.M. (2015, May 28). Stain Normalization Toolbox.
%Retrieved from: https://warwick.ac.uk/fac/sci/dcs/research/tia/software/sntoolbox/

%Macenko M, et al. "A method for normalizing histology slides for
%quantitative analysis", IEEE International Symposium on Biomedical Imaging:
%From Nano to Macro, pp. 1107-1110, 2009.

%Pathology Education Informational Resource Digital Library. (2013).
%Retrieved from: http://peir.path.uab.edu/library/index.php?/category/2

%Ruifrok AC, Johnston DA. Quantification of histological staining by color
%deconvolution. Anal Quant Cytol Histol 23: 291-299, 2001.

%Veta, M. (2015, Jun 8).  Staining-normalization. Retrieved from:
%https://github.com/mitkovetta/staining-normalization/blob/master/normalizeStaining.m

%% Normalize Histology Slides ------------------------------------------------------------------------
%Note: Method based on (Macenko, 2009) & (Khan, 2013)
clear all

%Reference OD matrix for H&E staining
Mref = [
    0.5626    0.2159
    0.7201    0.8012
    0.4062    0.5581
    ];% directly from (Veta,2013)


% Load Image, Convert to Double & Normalize
img=double(imread('insert image name here'))/255; %normalize to [0,1]; 255 is Io, the intensity
% of light entering the specimen

%% ---------------------------------------------------------------------------------------------------
%Optical Density (OD)
OD=-log(img);
%figure; imagesc(OD); title ('OD Image', 'FontSize', 28); axis image;

%Reshape Matrix & Apply Threshold to RGB Channels
```

```
ODR=reshape(OD,[],3);
beta=0.15;
ODmask = ODR(~any(ODR < beta, 2), :); %examine nonzero elements of array; from
%(Khan,2013)
ODmask = ODmask(~any(isinf(ODmask), 2), :);

%Calculate Eigenvectors to Create Plane
[V, D] = eig(cov(ODmask)); %code from (Khan,2013)
Plane = V(:,2:3); %eigenvectors(V) corresponding to two largest eigenvalues(D)

%Project OD Pixels onto Plane
Project=ODmask*Plane;

%Obtain Angle Between Point and First SVD Direction
angle = atan2(Project(:,2), Project(:,1)); %Note: this becomes a scalar; code from (Khan, 2013)

%Identify Angle Extremes
minang=prctile(angle,1); %From Khan,2013
maxang=prctile(angle,99);

%Convert to OD Space & Compute Stain Vectors for Hematoxylin & Eosin
V1 = Plane*[cos(minang); sin(minang)]; %Code adapted from Khan, 2013
V2 = Plane*[cos(maxang); sin(maxang)]; %Code adapted from Khan, 2013

%% Color Deconvolution to Hematoxylin & Eosing Specific Images ----------------------------------
%Note: Method based on (Ruifrok, 2001) & code from (Veta, 2013)

%Determine if V1 is Hematoxylin or Eosin
if V1(1) > V2(1) %code from (Veta, 2013)
   M(1,:)=V1; %V1 = Hematoxylin
   M(2,:)=V2; %V2 = Eosin
else
   M(1,:)=V2; %V2 = Hematoxylin
   M(2,:)=V1; %V1 = Eosin
end

%Transpose OD Matrix & y Values
M=M';
y=ODR';

%Calculate Stain Amount at Each Pixel
C=M\y; %from (Veta, 2013)

%Determine Image Size
size=size(img);
row=size(1);
```

```
col=size(2);

% Produce Separate Hematoxylin & Eosin Images
H = exp(-Mref(:,1) * C(1,:)); %from (Veta, 2013)
HR = reshape(H', row, col, 3);
%figure; imagesc(HR); axis image; title ('Hematoxylin', 'FontSize', 28);

E = exp(-Mref(:,2) * C(2,:)); %from (Veta, 2013)
E = reshape(E', row, col, 3);
%figure; imagesc(E); axis image; title ('Eosin', 'FontSize', 28);

%% Calculate Fibrin vs RBC Estimate in Eosin Image ----------------------------------------------------

%Convert Eosin Image to Grayscale
Egray= mean(E,3);
%figure; imagesc(Egray); colormap gray; axis image; title 'Gray Image of Eosin';

%Mask Image for White Spaces
thresh = 0.97; %qualitatively optimized by comparison of three atrial thrombi images
mask= E(:,:,1) < thresh;
%figure; imagesc(mask); axis image; colormap gray;

%Create Masks
thresh=0.87; Egray = E(:,:,1);
EmaskF=(Egray>thresh); %mask of fibrin components
EmaskRBC=(Egray<thresh); %mask of RBC components

EmaskF=EmaskF.*mask; %apply mask of white values to fibrin mask
EmaskRBC=EmaskRBC.*mask; %apply mask of white values to RBC mask
figure;
subplot (1,2,1); imagesc(EmaskF.*E); colormap gray; axis image; title ('Fibrin Mask', 'FontSize',
28);
subplot (1,2,2); imagesc(EmaskRBC.*E); colormap gray; axis image; title ('RBC Mask',
'FontSize', 28);

%Calculate Percent Fibrin and RBCs in Eosin Image
numpixF=sum(sum(EmaskF)); %number of fibrin pixels from mask
numpixRBC=sum(sum(EmaskRBC)); %number of RBC pixels from mask
prcF=numpixF/(numpixF+numpixRBC); %percent fibrin
prcRBC=numpixRBC/(numpixF+numpixRBC); % percent RBC

%Display Percentage Values
P=[prcF, prcRBC];
disp('    prcF    prcRBC'); %space required to align words over matrix P
disp(P);
```

```
%Validation of Appropriate Masks & Intensities
%Note: Fibrin stains lighter than RBCs; therefore, fibrin intensity should be greater
F= EmaskF.*Egray;
RBC=EmaskRBC.*Egray;

%figure; imagesc(RBC); colormap gray; axis image; title ('RBC', 'FontSize', 28);
%figure; imagesc(F); colormap gray; axis image; title ('Fibrin', 'FontSize', 28);

avgF=sum(sum(F))/sum(sum(EmaskF)); %avg intensity of fibrin
avgRBC= sum(sum(RBC))/sum(sum(EmaskRBC)); %avg intensity of RBC

if avgF < avgRBC
   error('Average intensity of fibrin is less than that of RBCs - double check code');
end
```

Appendix B: Composition Results for Individual Tissue Segments

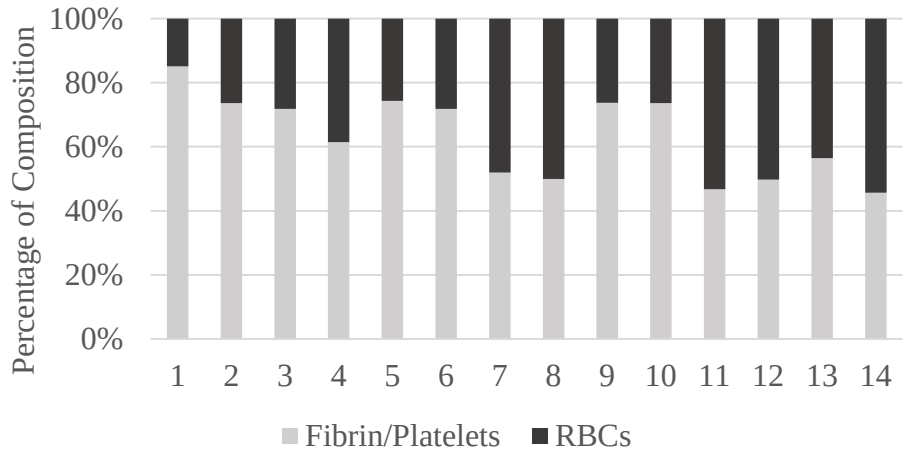

Figure B 1. Composition percentages for tissue samples from EAs formed at 34 RPM

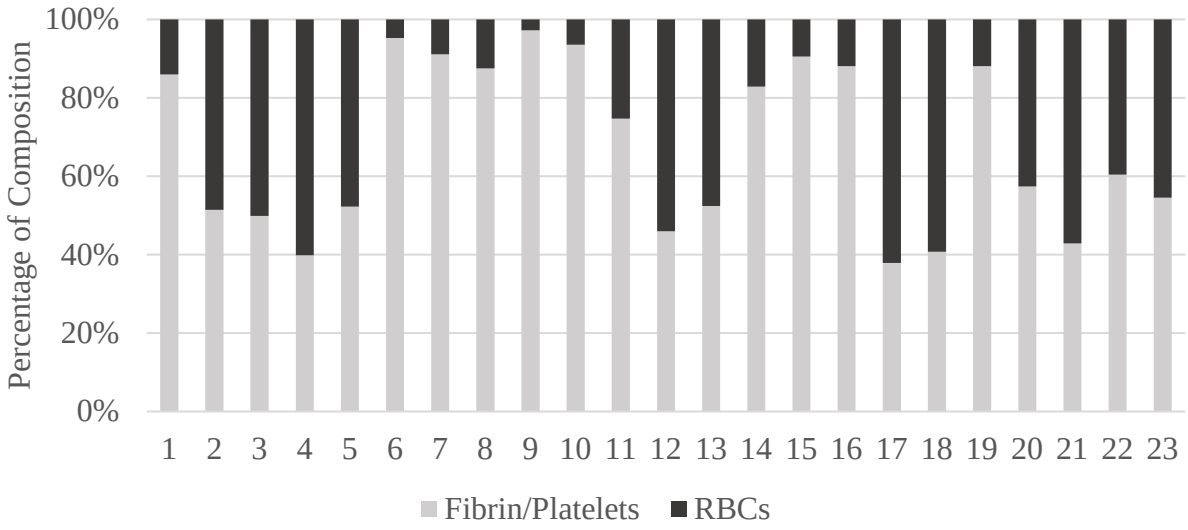

Figure B 2. Composition percentages for tissue samples from EAs formed at 50 RPM

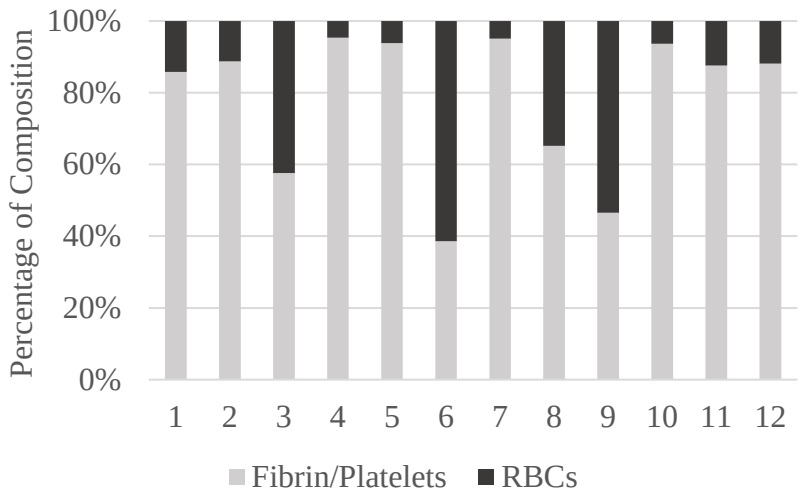

Figure B 3. Composition percentages for tissue samples from EAs formed at 80 RPM

Appendix C: Additional Figures of Non-linear Stress-Strain Graphs

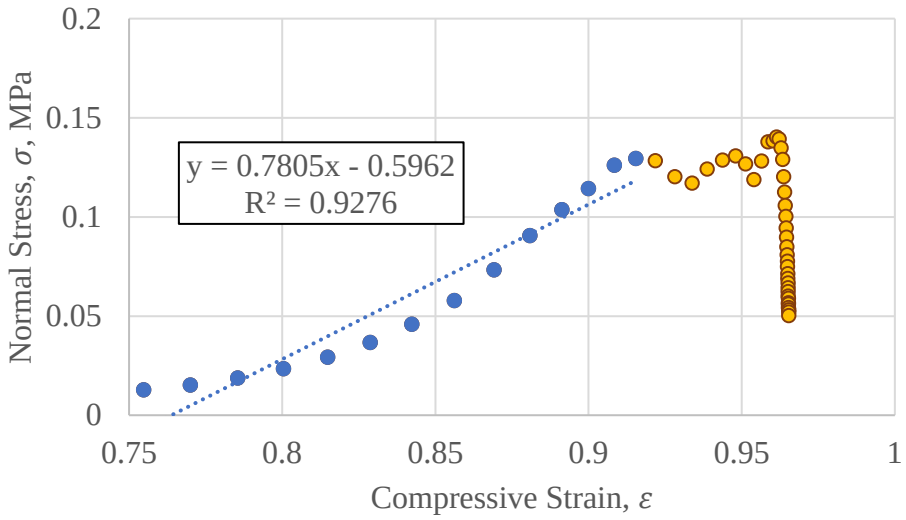

Figure C 1. Normal stress, σ, versus compressive strain, ε, for static EA tissue segment 195c.

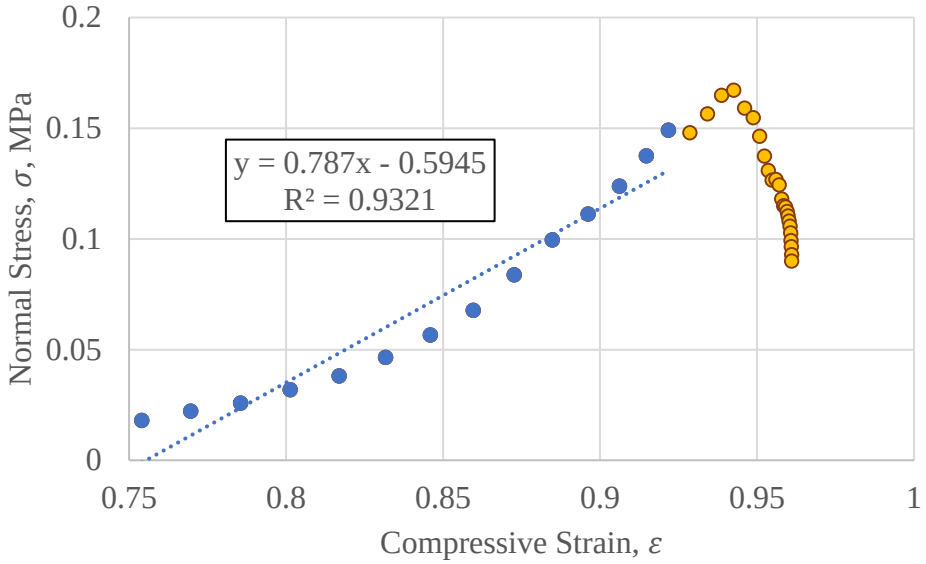

Figure C 2. Normal stress, σ, versus compressive strain, ε, for static EA tissue segment 196cb.

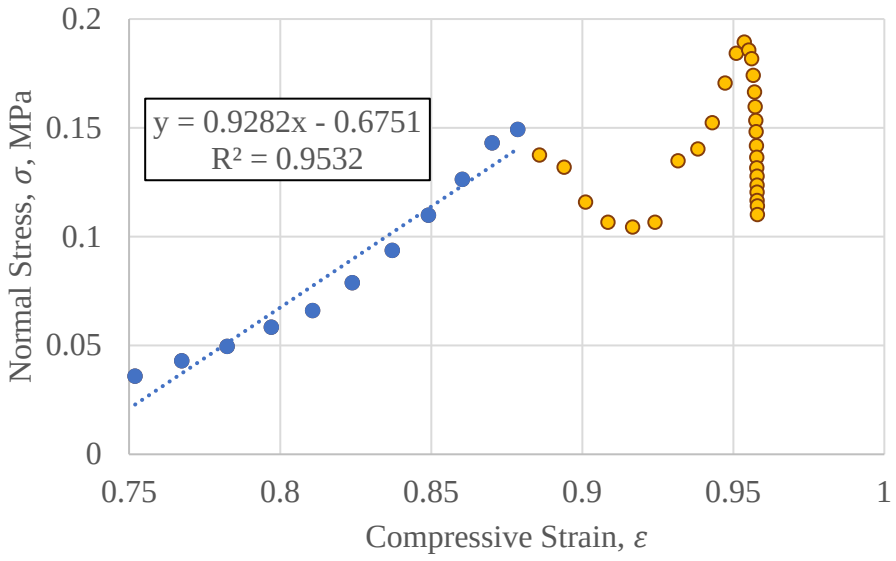

Figure C 3. Normal stress, σ, versus compressive strain, ε, for static EA tissue segment 197c.

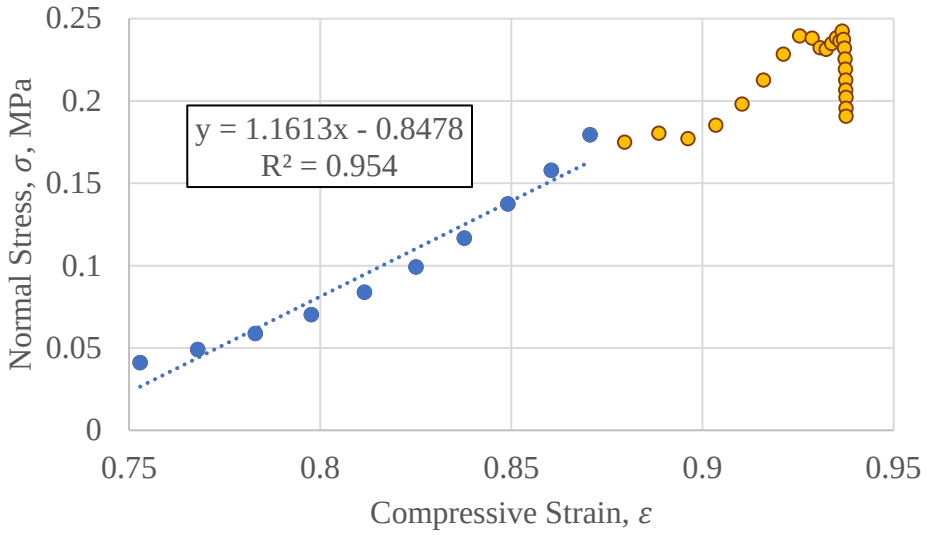

Figure C 4. Normal stress, σ, versus compressive strain, ε, for static EA tissue segment 198b.

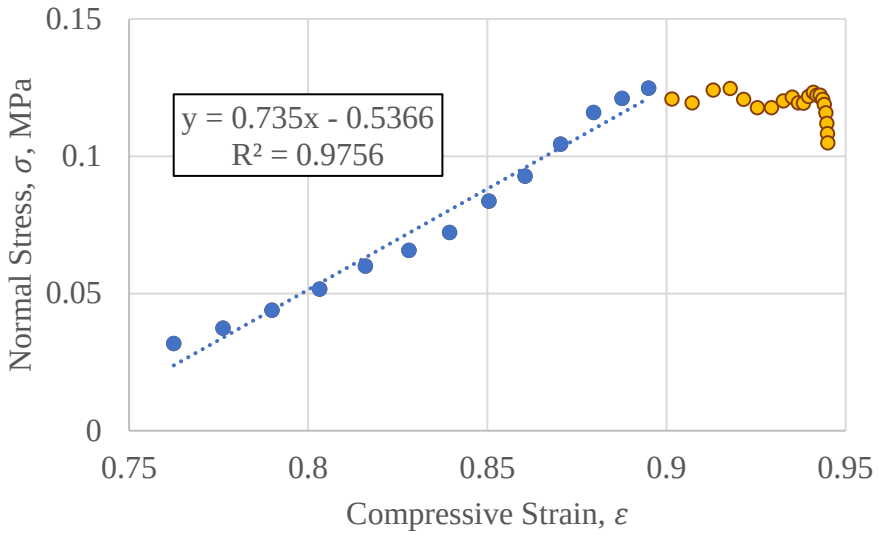

Figure C 5. Normal stress, σ, versus compressive strain, ε, for static EA tissue segment 198c.

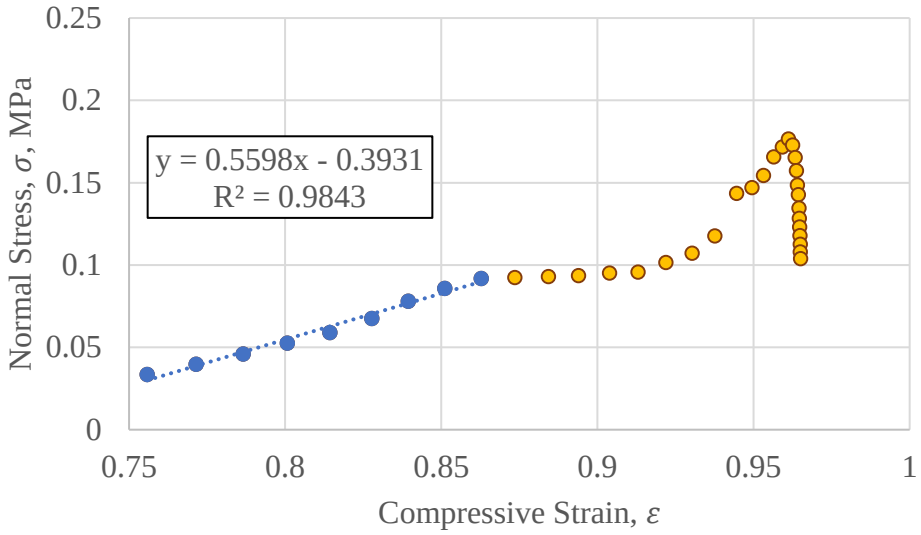

Figure C 6. Normal stress, σ, versus compressive strain, ε, for static EA tissue segment 197b.

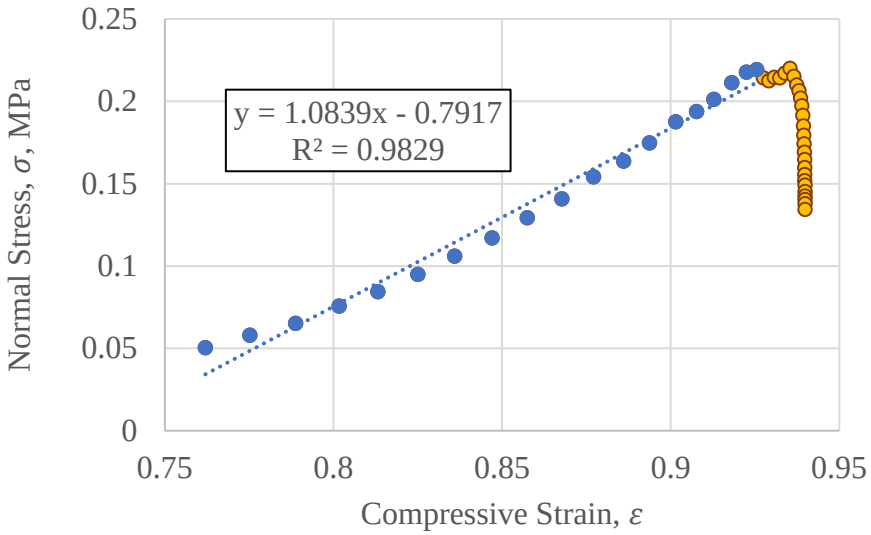

Figure C 7. Normal stress, σ, versus compressive strain, ε, for dynamic EA (50 RPM) tissue segment 142a.

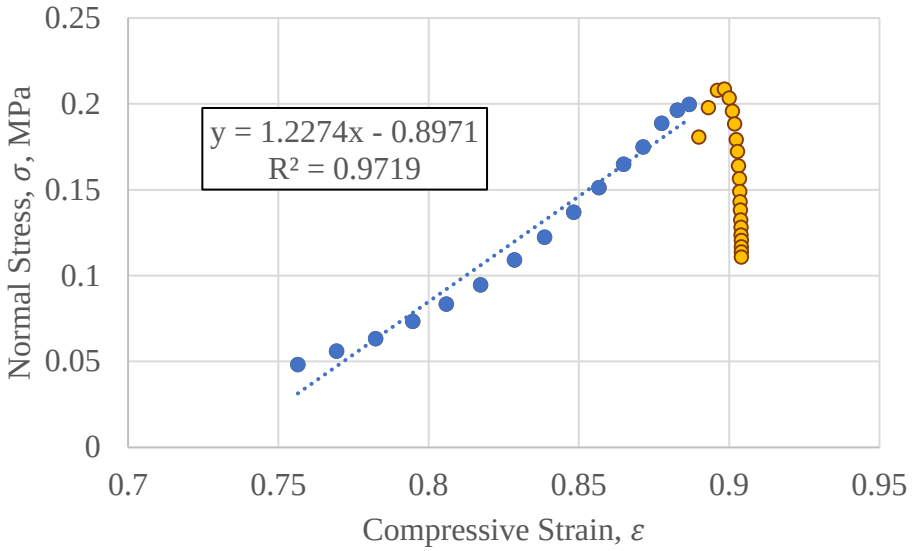

Figure C 8. Normal stress, σ, versus compressive strain, ε, for dynamic EA (80 RPM) tissue segment 18b.

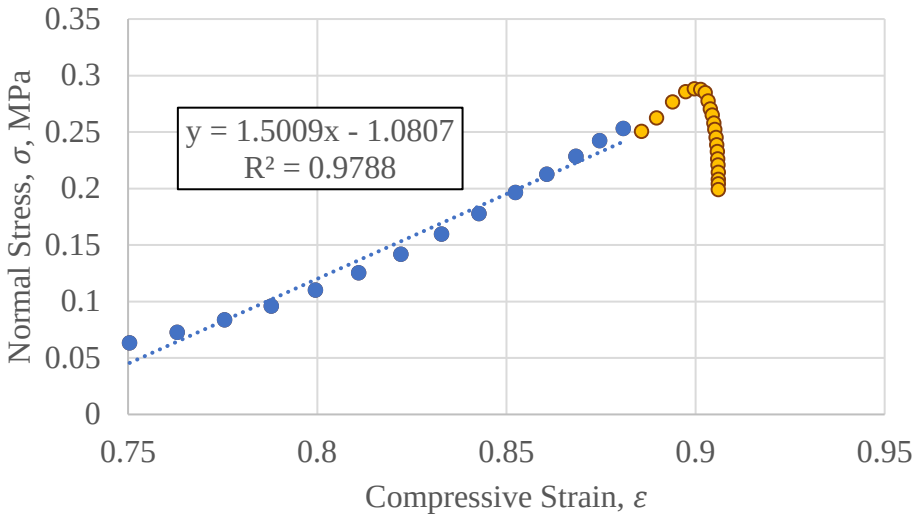

Figure C 9. Normal stress, σ, versus compressive strain, ε, for dynamic EA (34 RPM) tissue segment 162a.